INTERNATIONAL JOURNAL OF
IJCOE
COASTAL, OFFSHORE & ENVIRONMENTAL ENGINEERING

Volume 1 | Issue 3 | Oct 2016

www.ijcoe.org info@ijcoe.org 3

International Journal of Coastal, Offshore and Environmental Engineering (IJCOE) Vol. 1 / Issue. 3 / Oct 2016

International Journal of Coastal, Offshore & Environmental Engineering
Since 2015
ISSN: 2980-8731 (online)

Volume 1 | Issue 3| Oct 2016

IJCOE
Editor-in-Chief: Prof. Hamid S.Bahai

International Journal of Coastal, Offshore & Environmental Engineering
Since 2015
ISSN: 2980-8721 (online)

In The Name of God

Message from the Editor-in-Chief

The IJCOE journal office was established in 2015,and its first issue was published in 2016. TheIJCOE covers a wide range of research in thefields of oceanography & ocean technology, aswell as marine industries & marine engineering.The editorial board of IJCOE consists of nearly130 of the greatest scientists and researchersfrom over 30 countries worldwide, and thejournal's review board comprises 1,000 membersfrom all five continents. The membership andapplication process for joining the editorial andreview boards of this journal is ongoing. IJCOE isa research-academic quarterly journal that haspublication and distribution permissions fromthe Press Organization and permission topublish scientific-research articles from theMinistry of Science, Research, and Technology(MSRT) with an "A" rating. It also holds a "Q1"rating from the ISC institute with an impactfactor (IF) of approximately 0.43 and isconsidered a "core journal" (prestigious andoutstanding journal). IJCOE is an open-accessjournal and allows the download and receipt ofaccepted articles in full text for free. It respectsand adheres to copyright and COPE regulations.The journal's office operates 24/7, providingservices to researchers. In addition to publishinga regular quarterly journal, IJCOE has 16 specialissues on specific topics in preparation. It alsoprovides conditions for publishing specializedbooks, references, and handbooks. Moreover, itis ready to cooperate with the secretariats ofreputable international conferences to publishtheir selected and outstanding articles. IJCOEevaluates, appraises, and publishes books,articles, and the scientific achievements andfindings of esteemed researchers and scientistsworldwide who are innovating and conductingin-depth research in the "important and strategicfield of the maritime technology & Oceanengineering." It welcomes any form of jointcooperation with universities, research institutes,and related research centers at the national,regional, and international levels, and extends ahand for collaboration.

Classification of Editorial Board in IJCOE

Editor-in-Chief

Director-in-Chief

Deputy Editor

Executive Managers

English Text Editor

Technical Editor

International Editorial Board

National Editorial Board

Editorial Board Associate

Editorial Board Assistant

Guest Editorial Board

Advisory Board

Administrative Coordinator

Honorary Board Member

Methodology Advisor

Author Benefits

- Open Access
- Rapid Publication
- Thorough Peer-Review
- No Copyright Constraints
- Coverage by Leading Indexing Services
- Discounts On Article Processing Charges (APC)
- No Space Constraints, No restriction on the maximum length of the papers, number of figures or colors

INTERNATIONAL JOURNAL OF IJCOE COASTAL, OFFSHORE & ENVIRONMENTAL ENGINEERING

Aims of IJCOE

Hydrodynamics

Marine equipment

Structural mechanics

Ocean environmental predictions

Stochastic calculations Experimental

Automatic Control of Marine Systems

Scope of IJCOE

Marine Hazards

Ocean Acoustics

Naval Architecture

Ocean Engineering

Coastal Engineering

Marine Meteorology

Marine Earth Sciences

Underwater Technology

Marine Renewable Energy

Polar & Arctic Engineering

Marine Renewable Energy

Marine Geography & Geodesy

Marine Environmental Engineering

Automatic Control of Marine Systems

Hydro Physics & Physical Oceanography

Type of papers

- Case Studies
- Book Reviews
- Review Article
- Letters to the Editor
- Methodology Papers
- Editorials and Commentaries
- Response or Rejoinder Papers
- Perspective or Opinion Papers
- Conceptual or Theoretical Papers
- Meta-Analysis and Systematic Reviews
- Short Communications or Brief Reports
- Research Articles (Original Research Papers)

Scientific Research Journal

Ministry of Science, Research And Technology (MSRT)

Jurnal Ranking 2023: A

Ministry Of Science, Research And Technology (ISC)

Citation Impact 2022: 0.429

Quartile 2022 : Q1

Core Collection

IJCOE is a Member of

Cantact Us

Office 1 | Research Institute of Meteorology and Atmospheric Science

Address | Tehran, Shahid Kharrazi Highway, Pajoohesh Blvd, Research Institute of Meteorology and Atmospheric Science, Sand and Dust Storm International Research Center (SDS-IRC), No. 13, 1st floor.

Phone | +982144787652

Postal code | 13611-14977

website | www.rimac.ac.ir

Office 2 | Iranian National Institute for Oceanography and Atmospheric Science

Address | Tehran, Dr. Fatemi Gharbi St., Shahid Etemadzade St., No. 3, third floor.

Phone | +982166944873

Postal code | 13389 – 14118

website | www.inio.ac.ir

Email | Info@ijcoe.org

Website | www.ijcoe.org

Follow Us

www.ijcoe.org

INTERNATIONAL JOURNAL OF IJCOE COASTAL, OFFSHORE & ENVIRONMENTAL ENGINEERING

Volume & Issue:

Volume 1, Issue 3, October 2016

Number of Articles: 6

Content

INTERNATIONAL JOURNAL OF
COASTAL & OFFSHORE ENGINEERING
IJCOE No. 3/Summer 2016 (1-7)

Effect of External Water Flow on Response of Cylindrical Shell Subjected to Under Water Explosion

S. Jalili[1, 2], E. Shad[2,3], and M. Biglarkhani[2]

[1] *PhD Candidate, Mechanical Engineering, Tehran University, Tehran, Iran, sinajalili@ut.ac.ir*
[2] *Orooj Gostar Aria, Tehran, Iran, info@oga_group.com*
[3] *MSc. Student, Coastal Engineering, Qom University, Qom, Iran, ehsan.shad@ymail.com*

ARTICLE INFO

Article History:
Received: 9 Jul. 2016
Accepted: 15 Sep. 2016

Keywords:
UNDEX, Cylindrical Shell, Fluid-Solid interaction, AUTODYN

ABSTRACT

This article deals with response of cylindrical shell subjected to loading of Under Water Explosion (UNDEX) when water current is introduced to the surrounding environment. Cylindrical shells as one of main basic structural elements in construction of marine and submarine facilities are prone to UNDEX threat. Due to vicissitudes of conducting experiments in this field and also complicated inherent of fluid-solid interaction phenomenon, numerical models can be used as an effective tool for scrutinizing the problem. In this study, a submerged thin walled cylindrical shell and its surrounding water discretized by coupled shell Lagrangian elements and Eulerian cells respectively. Simulations are performed in AUTODYN hydrocode. For better perceiving of phenomenon, studies are done for two various explosive charge stand-off distances. Results show that introduction of flow to water, can tangibly change the symmetrical configuration of flow- less problem. Due to intricate interaction of water flow and explosion bubble, distribution of UNDEX overpressure and impulse is disturbed and this leads to un-symmetric deformation of cylindrical shell. Also amplitudes of deflection are reduced obviously by increasing flow velocity.

1. Introduction

Shell structures, especially cylinder ones have extensive usages in marine and submarine industries. Due to round geometrical shape of cylindrical shells, their resistance against lateral loading is relatively higher than other plane shell-plating structures. Main body of various submarine vessels can be approximated by cylindrical shell. Submerged cylindrical shells are exposed to tangible high hydrostatic pressures due to depth of sea. But sometimes these structures are prone to be threatened by Under Water Explosions (UNDEX). Level of pressures of UNDEX loadings is very higher than of hydrostatic water pressure and its substantial rapid dynamic behavior makes it very destructive phenomenon. UNDEX response evaluation and design of this type of structures is a main priority. Many nonlinear sources such as rapid large deformation of materials, interaction of structure-fluid (FSI) and large amount energy conversion lead to that structures' analysis subjected to UNDEX loading be a very complicated task. Analytical models cannot play an impressive role among various engineering methods and experimental procedures can be very tedious, expensive and dangerous tools for obtaining feasible results. Numerical simulations by careful consideration of meticulous aspects of this method and being cognizant about the complicacies are extant in UNDEX problem can be implemented as a trade-off way for exploring intricacies of UNDEX and FSI problems, simultaneously.

Numerous researchers devoted their efforts to investigate UNDEX problem and its effect on structures. Experimental method is a main and robust tool for this purpose. Some scaled down models of simple engineering problems have been testes in UNDEX pools. Usually, these researches are associated by numerical simulations. Hung et al.[1] investigated the dynamic response of cylindrical shells to under water blast empirically. They used a pool as a simulating medium for conducting UNDEX tests. Also a numerical study was accomplished using DAA approximate method for considering fluid-solid interaction. Cylindrical panel's deformation was studies by Ramajeyathilagam et al. [2] by experimental and numerical methods. DYNA3D code was implemented for numerical analysis. Some simplifications may aid analytical models to predict

structural response subjected to underwater blast. Dynamic buckling of stiffened shells under transient lateral shock wave loading surveyed by Pedron and Combescure [3]. Wierzbicki and Hoo fat [4] by analytical study assessed damage parameters of cylinders under impact and explosive loadings.

One of the basic and main assumptions in previous references is being calm and stationary condition of water that even is not mentioned explicitly in articles. Other nonlinearities involved UNDEX-FSI problem are enough to be not handled by ordinary engineering methods and if flow of surrounding water is introduced into model, some considerations will be necessary. Meanwhile water currents are relevant in ocean and river applications and their speed may be tangible in a way cannot be neglected in advance and accurate design stages. By this new problem definition, spherical propagation of incipient shock wave is not acceptable and simulations must be performed from initiation of explosive charge detonation. In recent years, numerical procedures have found their way in highly rated mechanics problems and their puissant in solution of this type of events makes them a relatively cheap and powerful tool for tackling such difficulties. Hydrocodes among a lot of numerical packages available commercially or written privately; are developed for engaging with problems such as: explosion, blast, impact, penetration or perforation. This new introduced problem may be handled by using AUTODYN hydrcode. By the best knowledge of authors, there is no published research that concerns explosion in flowing water and its effect on structures.

In this article using a high fidelity multi-physics numerical model prepared in AUTODYN environment, above discussed problem is analyzed. For modeling of explosion of TNT charges in water depth, JWL equation of state is utilized. Simulations are performed for various flow velocities and two stand-off distances are chosen for better perceiving the problem. Cylindrical shell as a very useful structure in marine application is assumed to be the target resisting against the UNDEX loading. Finally, results are graphed for more illustrative comparisons.

2 . Problem Description

A thin walled cylindrical shell with 300 mm, diameter, 1000 mm length and 2 mm thickness dimensions is selected for studying water flow in longitudinal direction effect on structure. Cylindrical shell made from 4340 steel. Inside of cylinder is assumed to be filled by atmospheric air. Due to symmetry respect to the plane parallel to current direction, only half of problem is needed to be modeled. Two 23 and 106 grams TNT charges are used to make UNDEX from two different 1 and 1.5 m stand-offs, respectively. Flow velocities are varied from 0 (stationary condition) to 6 (m/s). Figure 1 shows a schematic of proposed problem.

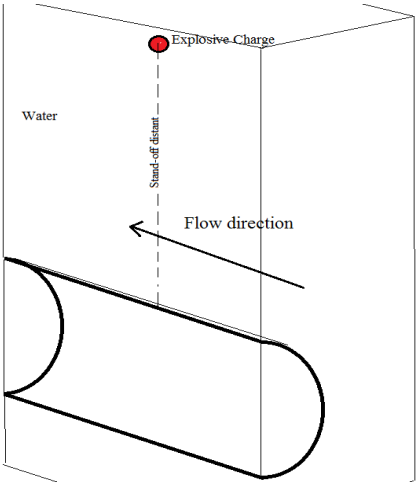

Figure 1: Problem Schematic.

3. Numerical Assessment

Explosive loading on structures usually associates with fluid-solid interaction phenomenon. High pressure of explosive detonation impacts adjacent particles of intermediate medium and the shock pulse propagates in environment. Nature of intermediate medium has serious effect on the history of explosive loading and must be counted in numerical procedures. Water as a relatively dense and incompressible environment makes some complicacies are not observable in air blast cases. So modeling surrounding water is necessary for getting accurate results. Explosion essence in water affected by incompressibility and after first shock loading, second and even third pulses consequence. First shock overpressure is very high but its endurance is short but in other hand second pulse has relatively long endurance and low overpressure amplitude making considerable impulse. Interaction of underwater shock wave with structure can be more intricate in comparison by air blasting loads. One of most important aspects of intermediate medium modeling is high deformation of fluids in comparison by structural elements. For avoiding distortion of fluid elements, Eulerian Approach must be utilized while Lagrangian method is suitable for capturing shell structures.

In this article, both of water and cylindrical structure are discretized by Eulerian cells and Lagrangian shell elements, respectively. For better tracking of FSI, Eulerian cells are refined in vicinity of structure. There are 324000 fine cells in water model while 3600 shell elements are employed for constructing cylindrical structure. Shell and surrounding Eulerian network are fully coupled.

Explosion is a highly nonlinear energy conversion event and for analyzing this problem, particular equation of states (EOS) are required. Accurate prediction of initiation of detonation in explosive material needs to fine grids may not be possible in 3-

D problems. Fortunately AUTODYN capability in modeling 1-D wedge problems may be implemented to reach highly accurate results. Incipient moments of explosion that deals with detonation wave propagation in explosive, may be simulated in 1-D wedge axial symmetry and results of this analysis can be remapped into high fidelity 3-D model. By means of this method there is no need to refine numerically high cost 3-D problem to visit fine grid requirements of detonation process. Figure 2 depicts numerically discretized model.

In cases, when loading is very rapidly applied on structures, behavior of structural materials can considerably modified particularly for metal ones. Steels are sensitive to high strain rate effect and this fact must be accounted in their numerical modeling. Johnson-Cook as a successful rate sensitive plasticity model for rates up to 10000/s, is implemented here for 4340 steel. Linear equation of state (EOS) is assigned to shell structural elements. Explosive charge that is assumed fabricated from TNT has very negligible mechanical strength and only a robust EOS is required. Often Jones-Wilkins-Lee (JWL) EOS has been utilized in literature for this purpose. In the case of water, polynomial equation of state can be a suitable one for handling fluid behavior in explosive loading. Required materials properties and related equations for sake of concise are tabulated in Table 1-4.

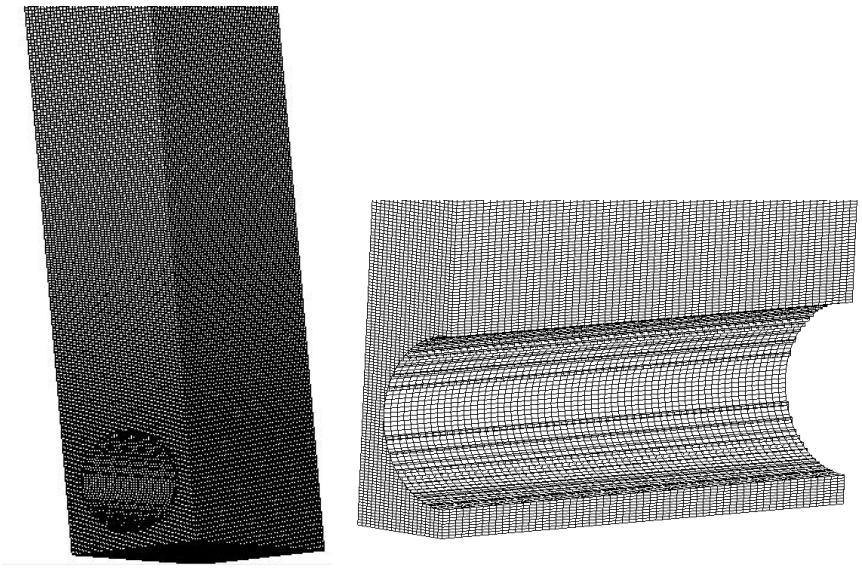

Figure 2: Numerically discretized model. (Left: Whole model mesh, right: magnified shell vicinity zone, note: Eulerian grids in internal portion of cylinder are omitted for sake of clarity)

Table 1. 4340 steel employed properties.

Mathematical relation and parameters definitions	Quantities of parameters
$\sigma_y = (A + B\varepsilon_p^n)(1 + C\log\varepsilon_p^*)(1 - T_H^m)$	A=792 MPa
$\sigma_y : Dynamic\ \ yield\ \ stress,$	B=510 Mpa
$\varepsilon_p : Effective\ \ plastic\ \ strain,$	C=0.014
$\varepsilon_p^* : Normalized\ \ plastic\ \ strain\ \ rate,$	n=0.26
$T_H^m : \frac{T - T_{room}}{T_{melt} - T_{room}}, normalized\ Temprature$	m=1.03
	T_m=1793 ^{0}K

Table2 . Linear Equation of State, 4340 steel.

Mathematical relation and parameters definitions	Quantities of parameters
p=Kμ p=Pressure	K=159 GPa
$\mu = \frac{\rho}{\rho_0} - 1,\ \rho : density$	$\rho_0 = 7830\ kg/m^3$

Table 3. Polynomial EOS for Water.

Mathematical relation and parameters definitions	Quantities of parameters
$p = A_1\mu + A_2\mu^2 + A_3\mu^3 + (B_0 + B_1\mu)\rho_0 e$	A_1=2.2 GPa
e: specific energy	A_2=9.54 GPa
μ: As defined in Table 2	A_3=14.57 GPa
	B_0=0.28
	B_1=0.28
	$\rho_0 = 1000\ kg/m^3$

Table 4. JWL EOS for TNT.

Mathematical relation and parameters definitions	Quantities of parameters
$p = C_1(1-\frac{\omega}{r_1 v})e^{-r_1 v} + C_2(1-\frac{\omega}{r_2 v})e^{-r_2 v} + \frac{\omega e}{v}$	C_1=373.7 GPa
	C_2=3.74 GPa
	r_1=4.15
	r_2=0.9
v= specific volume	$\omega = 0.35$
	$\rho_0 = 1630\ kg/m^3$

4. Results and discussions

After numerical calculations results presented in this part. Due to interaction of water flow with explosion bubble, spherical geometry of bubble deviated from symmetrical configuration and sphere of explosion gases elongated in flow direction, nominally. Also from resistance of flowing water in counter direction of bubble, a little increase of pressure observable in this side. By further propagating of UNDEX bubble, effect of flow enhanced and distribution of pressure will be more asymmetrical. Figure 3 shows a caption from normal view on symmetry plan of pressure field contour after progressing bubble roughly half way to reach shell. It is worth noting that departing from symmetrical loading is outstanding in velocities more than 4 (m/s). This may be returned to this fact that velocity field induced from UNDEX in shock front is in this order. Naturally by passing this velocity, flow dynamic pressure will have more puissant effect.

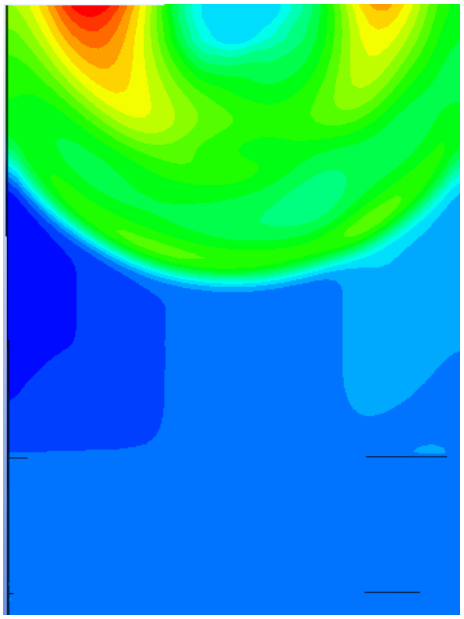

Figure 3: UNDEX bubble pressure field in 6(m/s) flow vel. *(Current direction from left to right)*.

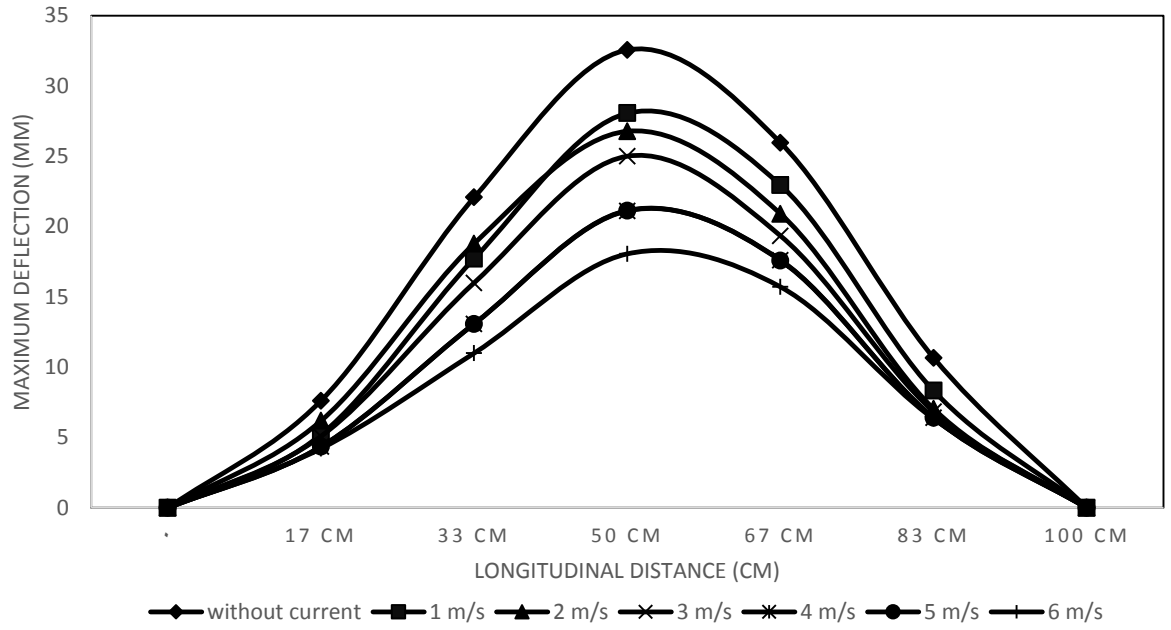

Figure 4. Deflection of symmetrical middle line of shell exposed to shock front for 1m stand-off and various flow velocities.

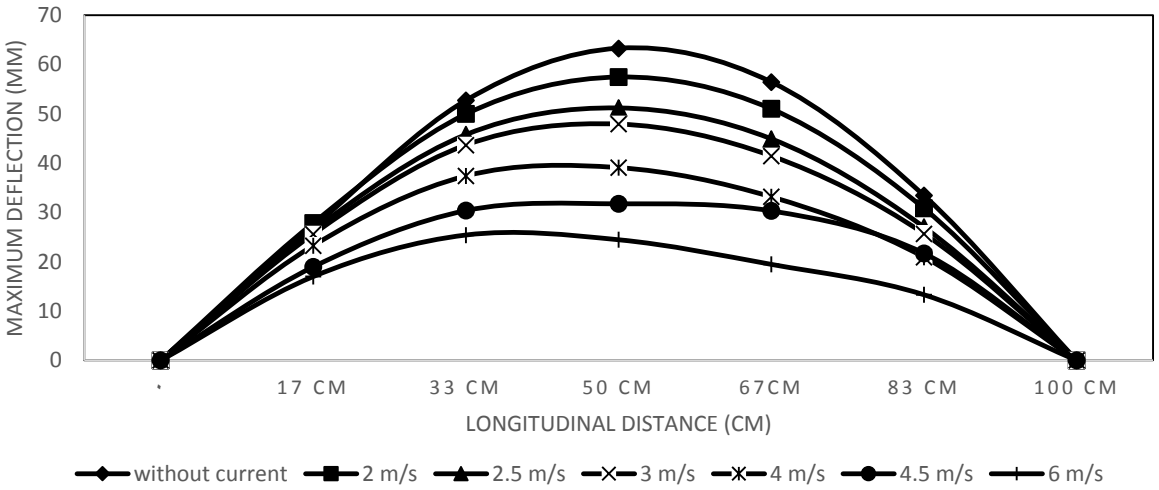

Figure 5. Deflection of symmetrical middle line of shell exposed to shock front for 1.5 m stand-off and various flow velocities.

Figures 4 and 5 depict variation of shell deflection for 1 m and 1.5 m stand-offs respectively, along the line located on the symmetry plane which is in side fronting shock wave of explosive charge. In flow-less case deflection function has a symmetrical configuration. By enhancing flow velocity, deflection apex deviates from center of graph and migrate to flow direction. This apex migration is more tangible for 1 m stand-off distance. This is due to nature of local distribution of pressure in near distant explosions. Deflection function also is sharper in this stand-off. As can be expected, energy of UNDEX absorbed by water current and fewer amount of energy imparted into the structure. So amplitudes of deflections are reduced significantly by escalation of flow velocity. Maximum of deflections for 6 m/s velocity is near to half of flow-less case.

In higher stand-off distant (1.5 m) deflection curve is flattened slightly. In farther distances of explosive charge standing, distribution of pressure are more uniform on entire of line of symmetry. As figure 5 shows, in this case up to 3 (m/s) current velocity, symmetry configuration of curve retained but by passing this velocity, a slight warping of curve is observable. In 4.5 (m/s) velocity a more robust symmetric curve is constructed again. This may be result of coincidence of UNDEX induced velocity and flow current velocity. At 6 (m/s) flow velocity more tangible deviation from symmetric curve is observed. But in this case maximum point of curve translates to counter direction of flow. Due to considerable complicacy of UNDEX bubble interaction with flow in various velocities, it is not easy task to justify this phenomenon, but stagnation of pressure in one side of bubble that confronts with flow velocity may produce

more overpressure in this side and more deformation morphed in this spot. For 1.5 m stand-off, reduction of deflections in 6 (m/s) is near to one third of flow-less case.

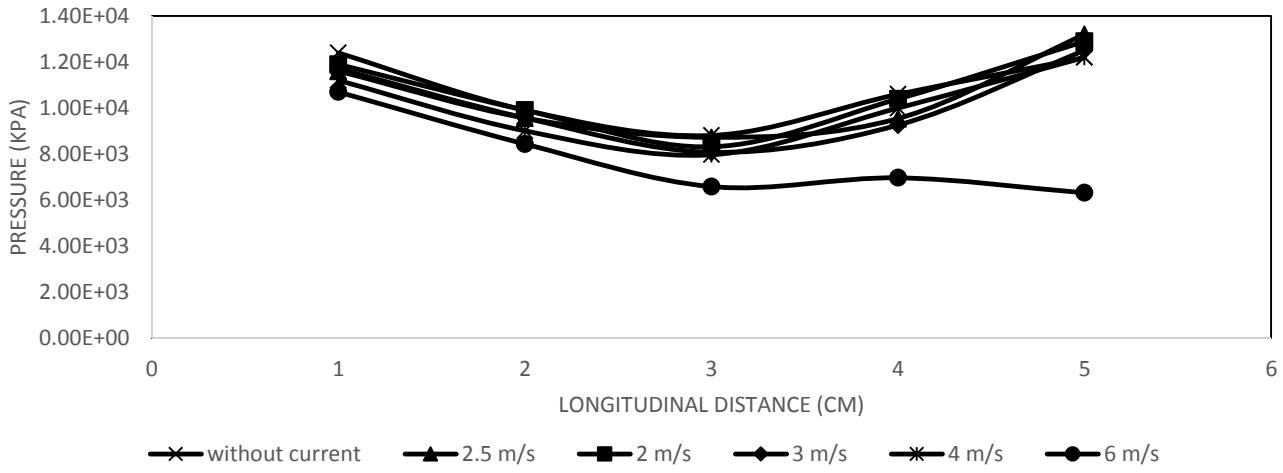

Figure 6. Pressure variation along symmetrical middle line of shell exposed to shock front for 1 m stand-off and various flow velocities.

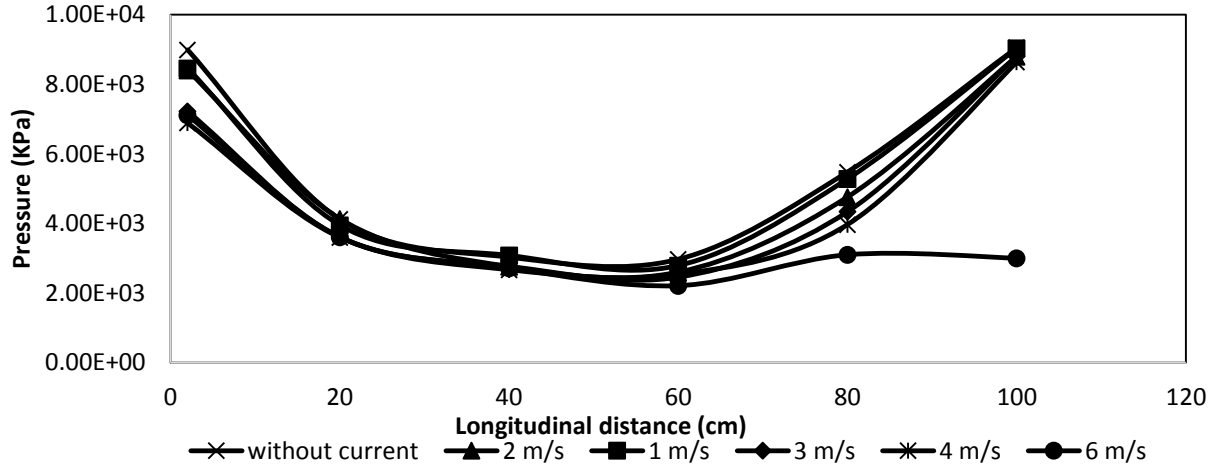

Figure 7. Deflection of symmetrical middle line of shell exposed to shock front for 1.5 m stand-off and various flow velocities.

Pressure variation along the symmetrical middle line at instant that maximum pressure is occurred, are illustrated in figures 6 and 7. As can be seen, peak pressure variation is not very sensitive to flow velocity. Only at 6 (m/s) a tangible deviation can be observed in exit port of current from model. Previous studies [5, 6, 7] have confirmed that peak pressure has not only main role in deformation of structures subjected to explosive loading. In other hand, time of applying pressure or its integration over time which is defined as impulse may be indexed as a noticeable parameter that causes to significant deformation of structures. Impulse in mathematical form can be shown as follows:

$$\mathrm{Im} = \int_0^{\infty} p(t)dt \qquad (1)$$

Above improper integral in explosive loadings converges to a specified quantity, because of exponential decadence nature of pressure history. For better perceiving pressure history of an underwater explosion, figure 8 proposes a sample graph. Because of incompressibility and higher viscosity of water, this history has intrinsic differences with its in air explosion (INEX) counterpart. Often after near distant and powerful UNDEX there are other pressure pulses interpreted as second, third and … pulses. Usually integration is done on a bonded time interval up to moment when pressure decays to zero. Figure 9 depicts variation of impulse for various flow velocities in two different stand-offs. As can be seen by increasing velocity, effective impulse will be subsided along the cylindrical shell. As integration over time makes fluctuations in time history weaker, there is no considerable change in spatial impulse profile along the shell and it seems this parameter for every current velocity is almost constant. It can be roughly construed that in farther stand-offs slop of

impulse curve vs. velocity is steeper, result of more time of bubble exposition to current and imparting its energy into the surrounding medium.

A three dimensional caption of deformed cylinder subjected to UNDEX in 6 (m/s) flow velocity and 1 (m) stand-off is shown in figure 10.

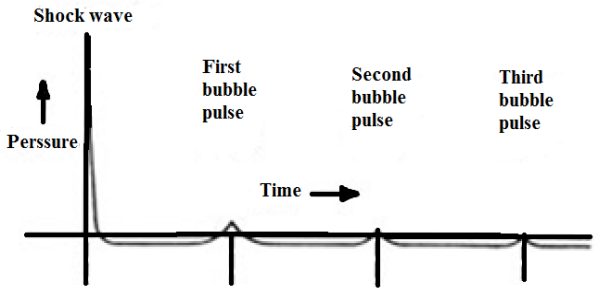

Figure 8. A sample UNDEX pressure history notice to second and third pulses resulted from oscillatory nature of bubble dynamics.

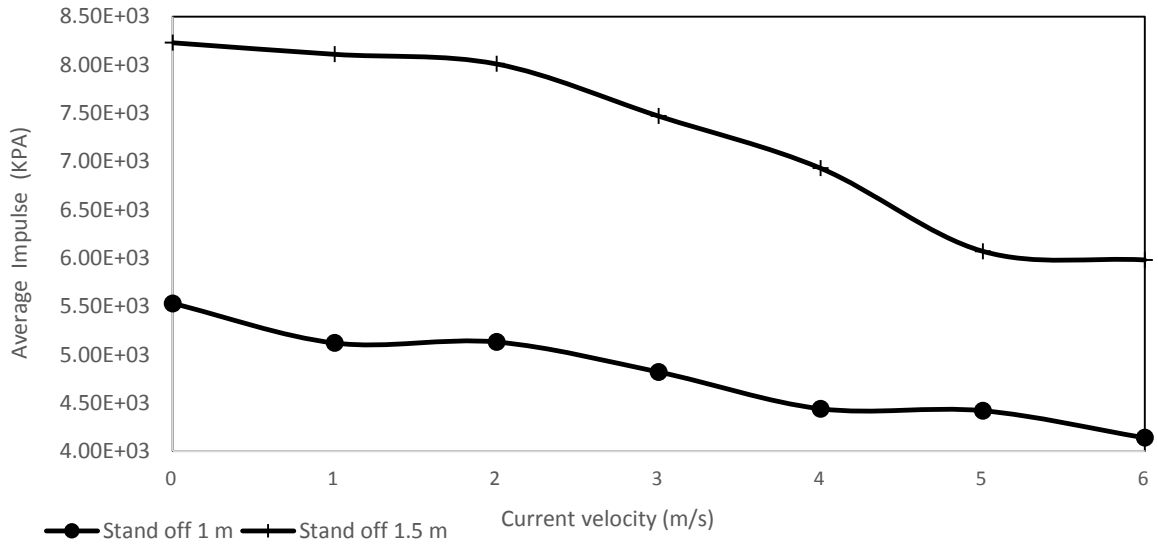

Figure 9. Variation of impulse as a function of surrounding water velocity, for two stand-offs. (*Note that for farther distant higher charge is used for more tangible deformation*)

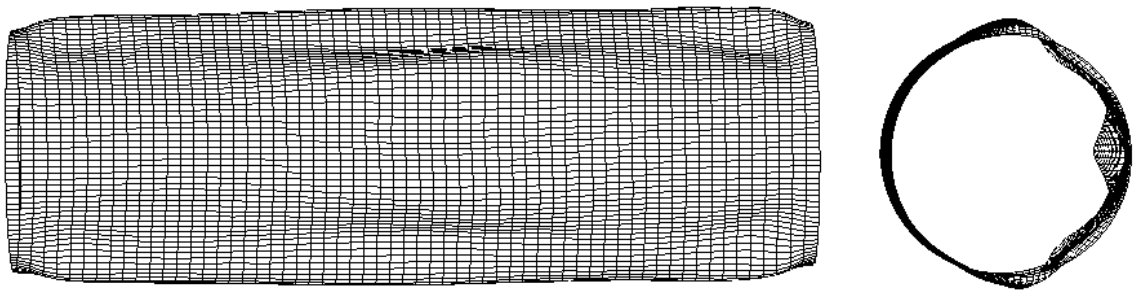

Figure 10. Three-dimensional embodiment of deformed shell in 6 (m/s) flow and 1 m stand-off.

5. Conclusion

A study for evaluation of water flow effect on UNDEX and FSI problem is fulfilled using high fidelity numerical procedure. As results show UNDEX phenomenon can be significantly affected by external flow. Furthermore, problem of FSI can be modified due to complicate interaction of UNDEX bubble, flow and structure. Investigation of numerical calculations illuminated that structural deformation morphology can tangibly be changed by introduction of external flow to surrounding medium. It is logical to be assumed that for UNDEXs with lower charges and farther stand-offs this effect can enhance. Finally, it is noteworthy that because of experimental challenges in conducting real scale tests for surveying water flow effect on UNDEX, numerical methods can be implemented successfully for better perceiving this elaborate problem.

References

[1] C.F. Hung, B.J. Lin, J.J. Hwang Fuu, P.Y. Hsu, “Dynamic response of cylindrical shell structures

subjected to underwater explosion", 2009, Ocean Engineering, pp. 564-577,

[2] K. Ramajeyathilagama, C.P. Vendhan and V. Bhujanga Rao, "Experimental and numerical investigations on deformation of cylindrical shell panels to underwater explosion", shock & vibration 8, pp. 253-268. 2001.

[3] Pedron, C., Combescure, A., "Dynamic Buckling of Stiffened Cylindrical Shells of Revolution under a Transient Lateral Pressure Shock Wave", Thin walled structures, 23, 1995, pp. 85-105.

[4] Wierzbiki, T., Hoo Fat, M., "DAMAGE ASSESSMENT OF CYLINDERS DUE TO IMPACT AND EXPLOSIVE LOADING", Int. J. of Impact Eng., 1993, 13, pp. 215-241.

[5] Safari, K.H., Zamani, J., Khalili, S.M. and Jalili, S., "Experimental, theoretical and numerical studies on the response of square plates subjected to blast loading", J. of Strain Analysis, 2011, pp. 805-816.

[6] Rajendran, R., Narasimhan, K., "Performance Evaluation of HSLA steel subjected to underwater explosion", J. Material Eng. & Performance, 2001, 10, pp. 66-74.

[7] Gupta, N.K., Kumar, P., Hegde, S., "On deformation and tearing of stiffened and un-stiffened square plates subjected to underwater explosion-a numerical study", Int. J. of Mechanical Sciences, 52, pp. 733-744.

INTERNATIONAL JOURNAL OF
COASTAL & OFFSHORE ENGINEERING
IJCOE No. 3/Summer 2016 (9-12)

Marine Forecasting Systems in Caspian Sea, Persian Gulf and Oman Sea

Aliasghar Golshani[1], Alireza Vaselali[2], Said Mazaheri[3]

[1]*MetOcean Expert, Beta Group Consulting Engineers; a.golshani@betagroupco.com*
[2]*Head of Design and Technology Department, Beta Group Consulting Engineers; a.vaselali@betagroupco.com*
[3]*Research Assistant Professor, Iranian National Institute for Oceanography and Atmospheric Science; said.mazaheri@inio.ac.ir*

ARTICLE INFO

Article History:
Received: 30 Jun. 2016
Accepted: 15 Sep. 2016

Keywords:
marine forecast
wind
wave
current
Persian Gulf
Caspian Sea, Oman Sea

ABSTRACT

There are several global marine forecast systems based on large scale regional data covering Iranian seas which are freely available on their websites. They are also several local marine forecast systems in Iranian waters. This paper performs an inter-comparison among different marine forecasting systems in Iranian seas in order to evaluate the accuracy and difference between them and give a proper ground for further investigation and research in this crucial issue. For this purpose, the results of two forecasting system in several points in the Persian are compared and the reason of differences are investigated.

1. Introduction

The marine forecasting is of great importance for several reasons including planning marine operations, scheduling shipping movements, dredging, survey, berth maintenance or construction. There are several global marine forecast systems based on large scale regional data which do not consider the localized effects of seabed and land topography on local wave and wind climate. They are also several local marine forecast systems in Iranian waters. This study aims to perform an inter-comparison among different marine forecasting systems in Iranian seas in order to evaluate the accuracy and difference between them and give a proper ground for further investigation and research in this subject.

Global Marine Forecast Project Covering Iranian Seas

MetOcean Solutions Ltd (MSL) operates a GIS tool for a 3-hourly 10-days wave forecasting namely WXTiles which does not include closed seas such as the Caspian Sea [1].

NOAA Environmental Modeling Center operates a 3-hourly 7-days wave forecast project using WWIII wave model and 0.5 degree GFS wind boundary conditions in Indian Ocean including Oman Sea and half of the Persian Gulf [2]. This project provides wind sea, primary and secondary swell parameters separately as output as well as spectrum, sources and bulletin in several point in Indian Ocean. Figure 1 shows NOAA Indian Ocean forecast in one time step for instance.

ECMWF Company provides three global wave forecast projects namely HRES-WAM (10 days, 0.25 degree), HRES-SAW (10 days, 0.125 degree) and ENS-WAM (15 days, 0.5 degree) by running WAM Cy41r1 model which are not freely available [3]. They do forecast every 3 hrs for the first 6 days and every 6 hrs afterwards.

Iranian Authorities Forecasts in Iranian Seas

Currently, there are three different authorities which are performing wave forecasts in Iranian Seas.

Iranian Meteorological Organization (IRIMO) runs a 6-hourly 4-days wind and wave forecast system in Iranian seas. They first run a WRF local wind model with resolution of 10 km using GFS boundary condition and the output is the input to a SWAN wave model with resolution of 2.5km to generate wave field [4]. There is two open boundaries in Oman Sea wave model (18N, 66E) without applying any boundary conditions.

Iranian National Center for Ocean Hazards (INCOH) at Iranian National Institute for Oceanography (INIO) runs a 6–hourly 4-days wave forecast system in Iranian seas using WWIII wave model (spatial resolution 0.05 degree) forced by GFS wind boundary condition [5]. There is an open boundary at 15N without applying any boundary condition.

Isfahan Technical University (ITU) performs a 6-hourly 4-days wave forecast system for Ports and

Maritime Organization (PMO) in Iranian seas using WWIII wave model forced by GFS wind boundary condition which uses the same method that INCOH uses for wave forecasting [6]. They have validated their forecast model by comparison with those of DHI forecast in Persian Gulf [7].

K.N. Toosi University (KNTU) with cooperation of Institute of Geophysics (IG) is currently working on a wave and 3D current forecast system in the Persian Gulf for PMO. They plan to run a WRF local atmospheric model with resolution of 0.1 degree and the wind and pressure output will be forced to PMO-Dynamics in-house wave and 3D current models [8].

Foreign Companies Forecasts in Iranian Seas

MSL operates a local 3-hourly 7-days wave forecasting namely SwellMap for Persian Gulf which provides swell wave parameters for recreational activities [9].

Based on PERGOS hindcast project, Danish Hydraulic Institute (DHI) with cooperation of OceanWeather Inc (OWI) runs a 3-hourly 7-days wave and current forecast in the Persian Gulf and Strait of Hormuz [10]. They use a modified NCEP wind field with spatial resolution of 0.75 degree as boundary condition which is adjusted using ship observations, QuikSCAT wind data and synoptic wind stations. Mike21 SW is run for wave forecasting and Mike21 HD 3D model for current and water level forecasting. The spatial resolution varies from 8 km offshore to 1 km near-shore. The output includes wave parameters, current speed and direction in different depth layers, and water surface level. Their results with coarse resolution is available on its website in time series, animation and tabular formats.

Turkish State Metrological Service (TSMS) runs a 3-hourly 5-days wind and wave forecast project in Caspian Sea [11]. They first run a MM5 local wind model with resolution of 4.5km (inner domain), 13.5 km (outer domain) using 0.15 degree ECMWF IFS boundary condition and the output is the input to METU3 in-house wave model with resolution of 3 km.

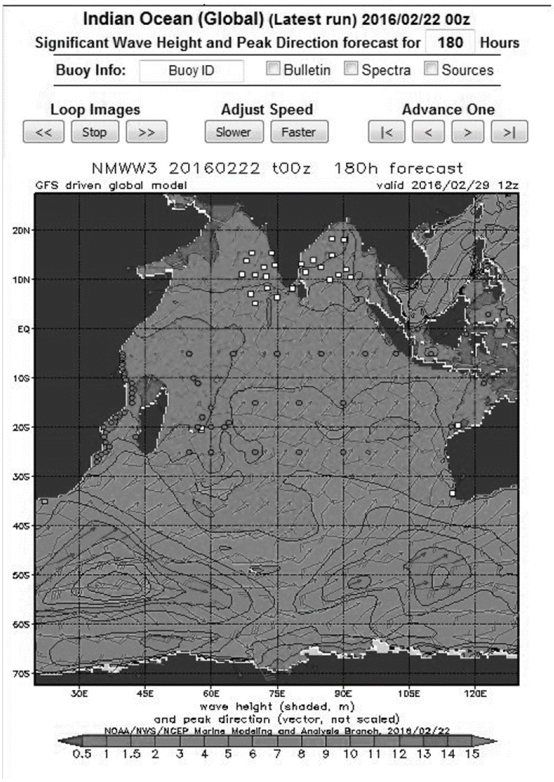

Figure 1: NOAA forecast in Indian Ocean

Results and Discussion

We can categorizes all above-mentioned forecasting systems in four main groups as below:

The first group is global forecast systems which uses coarse wind fields as input and run wave models with relatively coarse resolution (MSL, NOAA, and ECWMF). Their results are not accurate in closed seas like Caspian Sea and Persian Gulf especially when there are surrounded by high mountain ranges like south of Caspian sea, however they work well in the open oceans.

The second group is local systems which use coarse global wind fields as input to local wave models with fine resolution (INCOH, PMO-ITU). Wind field as the main driving input for wave model is not improved in these systems therefore, the wave results are still not accurate despite the implementation of finer mesh resolution and better bathymetry resolving in the wave model.

The third group is the local systems which use modified global wind fields as input to local wave models (DHI-OWI).

The fourth group is the local systems which run both wind model and wave model with fine resolution (IRIMO, TSMS, KNTU-IG). They use global wind forecasts (GFS, IFS) as boundary condition for the local wind models.

The 3rd and 4th groups are the most accurate systems in our area and it is recommended to use them for forecasting purpose (IRIMO for all Iranian seas, DHI-OWI for Persian Gulf, TSMS for Caspian Sea).

The time series of the forecast data are only presented by DHI (covering only Persian Gulf) and INCOH (covering all Iranian seas) websites, therefore it is only possible to compare the time series from these two forecast projects in the Persian Gulf. For instance, Fig.1-3 illustrate the comparison between DHI (belongs to G3) and INCOH (belongs to G2) forecasts in south of Qeshm Island, vicinity of Bushehr port and Asaluyeh areas, respectively. DHI forecast is higher in Qeshm, as DHI's wind in Strait of Hormuz is higher and more accurate (CC=0.85,bias=0.3m). INCOH's coarse GFS wind field is underestimated as this island is not well resolved in the wind model due to coarse land-sea mask and as a result high and unreal surface roughnesses in both sides of the strait. As for Bushehr Port, although two comparison points are 15 km away but results look very different and the reason for such a difference needs to be investigated. At Asaluyeh, despite their similar wave time series pattern, DHI point is located onshore while INCOH point is located offshore and they are 22 km away. This implies the necessity of application of a well-calibrated fine resolution model in Iranian waters via improvement of available forecasting systems for operational purposes.

Recommendation

For forecasting in Oman Sea, it is recommended to apply spectral or parametric wave boundary condition in open boundary or alternatively extending the Oman Sea mesh to cover the whole Indian Ocean to be able to capture properly the swells coming from the South Pole. Neither of the local forecasts have considered the open boundary conditions. NOAA Indian Ocean forecast model is extended to South Pole and has no open boundary.

It is also suggested to plot the buoys data in a graph together with forecast data and put them in the forecasting website for comparison between "the forecast results and what is happening in reality in the seas" purpose. It is worthy to mention that IRIMO and PMO has 10 and 7 operating buoys in Iranian Seas, respectively [12, 13] which can be used in this regards. Figure 5 shows the location of these buoys in Iranian waters.

References

[1] http://www.wxtiles.com
[2] http://polar.ncep.noaa.gov/waves
[3] http://www.ecmwf.int
[4] http://www.irimo.ir
[5] http://www.inio.ir
[6] http://waveforecast.pmo.ir/
[7] Saeidi, D., Zamani, A.R., Sedaghat, A., and Saghafian, M.," Validation of short-time wave forecasting in Persian Gulf , Oman Sea and part of Indian Ocean by using Iranian numerical wave prediction model", Proceeding of ICOPMAS2014.
[8] http://www.pmo.ir
[9] http://www.swellmap.co.nz/
[10]http://gulf.waterforecast.com/dbm/DashboardEngine.aspx?DashboardID=Gulf\Home
[11] http://www.mgm.gov.tr/en-us/marine-metu3-detail.aspx?g=p&b=Hazar
[12] http://buoy.irimo.ir/
[13] http://marinedata.pmo.ir/

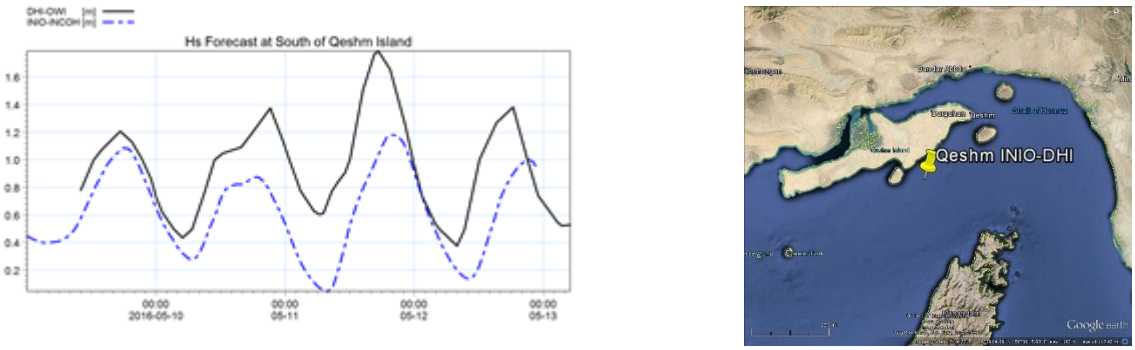

Figure 2 Comparison between DHI and INCOH forecasts at Qeshm

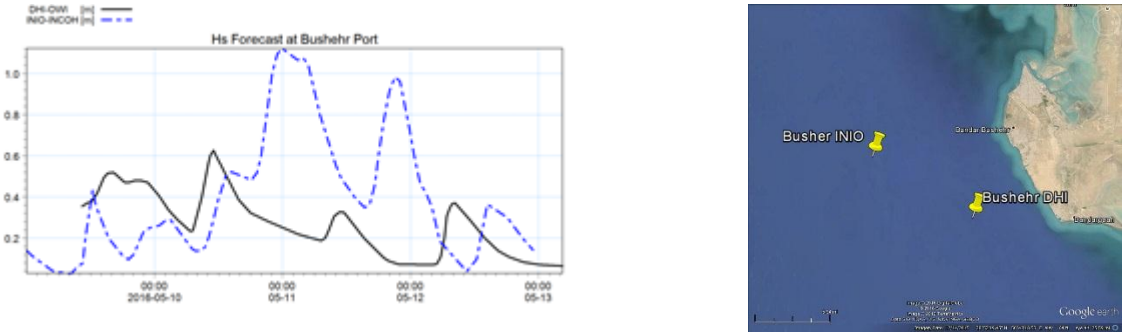

Figure 3 Comparison between DHI and INCOH forecasts at Bushehr

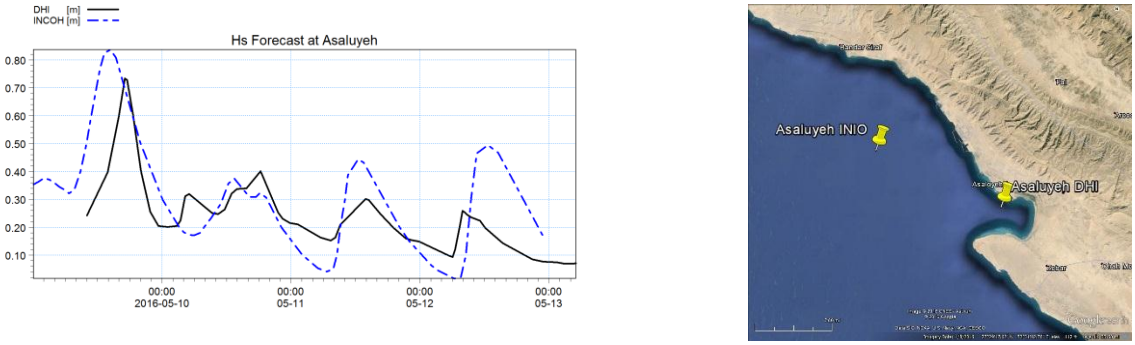

Figure 4 Comparison between DHI and INCOH forecasts at Asaluyeh

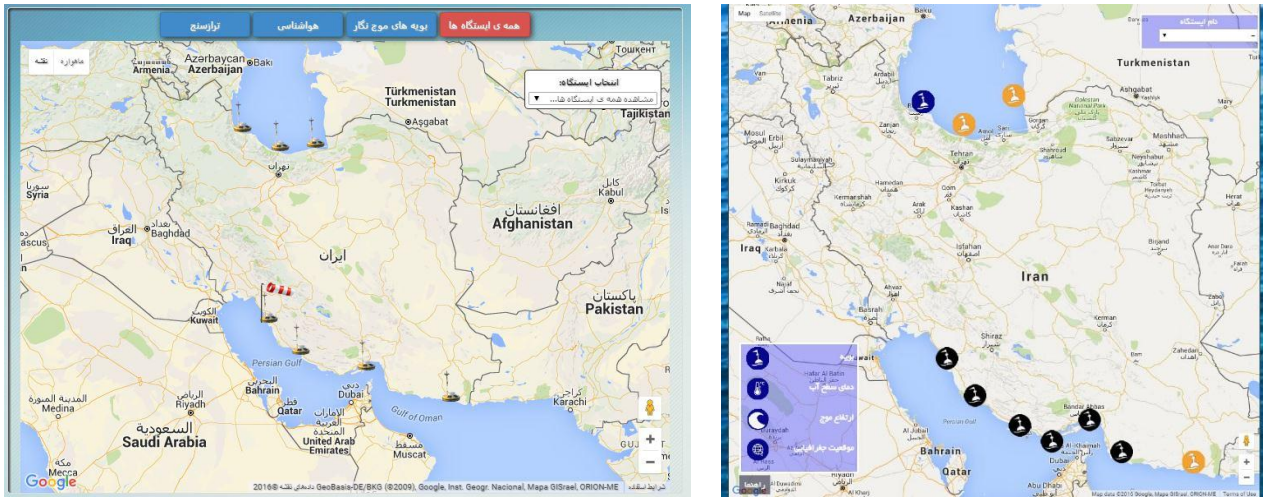

Figure 5 Location of operating buoys in Iranian Seas (left belongs to: PMO, right belongs to: IRIMO)

INTERNATIONAL JOURNAL OF
COASTAL & OFFSHORE ENGINEERING
IJCOE No. 3/Summer 2016 (13-18)

Cross-Flow Vortex Induced Vibration Fatigue Analysis of Persian South Gas Field Subsea Pipelines Due to Multi-Spanning

Mahdi shabani[1], Abdolrahim taheri[2]

[1] *M.Sc. student of Petroleum University of technology, department of offshore engineering;* m.shabani@mnc.put.ac.ir
[2] *Assistant- Prof. of civil Petroleum University of technology, department of offshore engineering;* rahim.taheri@put.ac.ir

ARTICLE INFO

Article History:
Received: 24 May. 2016
Accepted: 15 Sep. 2016

Keywords:
subsea pipelines, fatigue analysis, natural frequency, multi spanning, vortex shedding

ABSTRACT

Free-span in subsea pipelines occur at manmade supports, uneven seabed or pipeline crossing. Free spanning may induce pipeline vibration due to vortex shedding which makes pipeline susceptible to some failures such as fatigue, fracture, etc. Free spanning analysis is an important subject because fatigue is the most effective factor in reducing the pipeline design life. Free spanning analysis includes static analysis and dynamic analysis.
DNV-RP-F105 suggests a methodology of dynamic analysis for long pipeline with multi-mode responses, but the fatigue analysis method for multi-modes is not detailed. In addition, the fatigue analysis of multi-spanning pipeline is not clear. Based on the methodology of DNV-RP-F105 fatigue life relates to natural frequencies of pipeline, the method of determination of effective natural frequencies still is not clear.
In this paper, a fatigue analysis for multi-spanning pipeline in Persian south gas field is performed based on VIV analysis. ABAQUS FE model is developed to obtain the stress distribution and the natural frequency of each vibration mode for spanning pipeline on seabed with three multi-spans, then the fatigue analysis of VIV is carried out for the spanning pipeline based on DNV-RP-F105.

1. Introduction

Based on the high amount of subsea pipelines in transferring crude oil from wells to offshore platforms and also in exporting oil and gas from offshore facilities to onshore terminals, they play an undeniable role in offshore industries. As depth increase, the cost of repairing or replacing the linepipes is growing up, so assessment and exploration of what cause to decrease pipeline's serviceability lifetime is too much important in budget of project. Submarine pipelines can be laid on seabed in various methods (which depend on the basis of design (BOD)) either embedded in a trench (buried form) or laid on uneven seabed (unburied form). Because of the short time construction and economic consideration, unburied form is more common. In this method, however, the pipelines are subjected to some severe factors such as: free spanning, fatigue, fracture, etc. Free spanning mainly occurs as a consequence of uneven seabed and local scouring due to flow turbulence and instability (which is a resultant of artificial supports or pipeline crossing). Fatigue is the main consequence of free spanning. Resonance as main source of fatigue happens when external load frequency equal to the pipe natural frequency. Because fatigue is the most effective factor in decreasing design life time, free spanning analysis is an important item for designing subsea pipelines. DNV (2006) recommend a methodology for dynamic analysis of free spanning for long subsea pipelines, but number of Natural Frequencies for determination fatigue life is not clear.
In this study, ABAQUS software has been used to simulate structural response of subsea pipeline of 22th phase of South Persian Gas Field by considering three equal spans. Then the MATLAB software is used to calculate the fatigue life capacity due to Eigen frequencies and stresses based on the ABAQUS analysis results in cross-flow direction.
The following steps are performed to obtain the VIV fatigue damage of the subsea pipeline:

- Cross-flow Eigen frequencies and mode shapes are calculated at crossing.
- Fatigue life damages are calculated with Eigen frequencies and unit stress amplitudes in the

MATLAB software and then fatigue life can be calculated according to corresponding fatigue damages.
Finally, fatigue life is calculated by considering each natural frequency and effect of natural frequencies on fatigue life time is assessed.

Finite Element Model

The pipeline is modeled as a 3D beam with PIPE31. Seabed and crossing supports were modeled with rigid surfaces by disregarding the pipe embedment for conservatism. Both ends of the pipe were fixed axially after the pipeline was completely laid down on the seabed with a nominal residual bottom-tension force. In the load steps, the pipe gravity force is applied to the model first, followed by the internal pressure, external pressure, and temperature to match the effective axial force [2].
After the model has been set at the appropriate loading directions, natural frequencies in the cross flow directions and corresponding mode shapes can be obtained.
The following aspects should be considered in the pipeline model:

- The pipeline coating effect is limited only to increase the pipeline submerged weight, drag forces, added mas and buoyancy, the stiffness and strength increase has been neglected.
- The pipeline element length should be in the order of the outer diameter of the pipeline.
- The boundary condition at both ends of the pipe model shall accurately represent the pipe-soil interaction and the continuity of the pipeline.
- Sufficient pipe model length at both sides of the span should be created to account the effect of adjacent spans.

Fatigue Damage

The fatigue damage due cross-flow VIV is calculated based on DNV-RP-F105, the following fatigue criterion which is limited to stress cycles within the elastic ranges can be used for subsea free spanning pipeline fatigue assessment[[2][7]]. The fatigue criterion can be formulated as:

$$\eta . T_{life} \le T_{exposure} \text{ [1]} \qquad (1)$$

It is clear that the fatigue design life capacity must be longer than the exposure duration[3]. The relationship between the fatigue design life capacities, exposure time and fatigue damage is:

$$D_{fat-damage} = \frac{T_{exposure}}{T_{life}} . \eta \text{ [1]} \qquad (2)$$

Cross-Flow VIV Fatigue Assessment for Multi-Mode Response

For subsea pipeline, the multi-span and multi-mode scenario, Cross-flow VIV fatigue life calculation procedures can be summarized as below based on DNV-RP-F105 [2], [6]:

- Gather the input data, including the pipeline design/operation data, soil data and environment data.
- Calculate the still water cross-flow Eigen frequencies $f_{i,cf-still}$ by ABAQUS
- Find out the dominant cross-flow mode (i="Dominant") for each span length at flow velocity V_k (k=1 for the first step and the range is k=1,2,…,l^*),i.e. the largest cross-flow with the largest A_{Z_i}/D value (A_{ZDom}/D) predicted from the response model for velocity V_k, then the "weak" and "negligible" cross flow mode can be determine by:

$$i = \begin{cases} "weak" & for \quad A_{Z_i}/D \ge 10\% \, A_{ZDom}/D \\ "negligible" & for \quad A_{Z_i}/D < 10\% \, A_{ZDom}/D \end{cases}$$

[1][6] (3)

- Calculate the stress induced at the cross-flow mode in the pipe location x_j (j=1,2,…,n^i) along the span length for each cross-flow mode i (i=1,2,…,n^*) by the following formula:

$$S_{i,cf}(x_j) = \begin{cases} 1.2.A_{i,cf}(x_j).\left(\frac{A_{zi}}{D}\right).R_k.\gamma_s & i = "Dominant" \\ 0.5.2.A_{i,cf}(x_j).\left(\frac{A_{zi}}{D}\right).R_k.\gamma_s & i = "weak" \\ 0.0 & i = "negligible" \end{cases}$$

[1]] (4)

Where $A_{i,cf}$ is obtained by ABAQUS stress output report and A_{Z_i}/D can be calculated based on the Cross-flow response model is shown in "Figure 1".

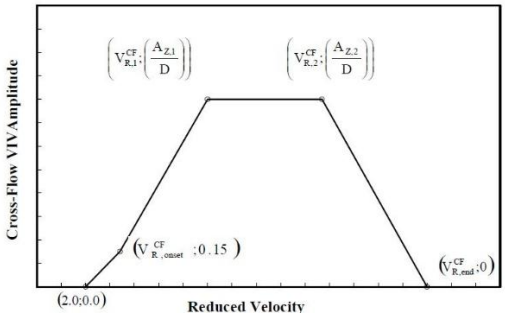

Figure 1: Cross-flow response model generation principle [4]

- Calculate the combined cross-flow induced stress at the location x_j (j=1,2,…,m*) along the span length by the following formula:

$$S_{comb,cf}\left(x_j\right)=\sqrt{\sum_{i=1}^{n^*}\left(S_{i,cf}\left(x_j\right)\right)^2}\ [1][1]] \qquad (5)$$

- Calculate the cycle counting frequency for this combined cross-flow induced stress at the location x_j (j=1,2,…,m*) along the span length by the formula below:

$$f_{cyc,cf}\left(x_j\right)=\sqrt{\sum_{i=1}^{n} f_{i,cf}\frac{S_{i,cf}\left(x_j\right)}{S_{comb,cf}\left(x_j\right)}}\ [1][1] \qquad (6)$$

Where:

$$f_{i,cf}=\begin{cases} f_{i,xf-RES} & for\ \ i="Dominnant" \\ f_{i,cf-still} & for\ \ i="weak" \\ 0 & for\ \ i="negligible" \end{cases}\ [1][1]] \qquad (7)$$

$$f_{i,cf-RES}=f_{i,cf-still}\sqrt{\frac{\left(\rho_s/\rho\right)+C_a}{\left(\rho_s/\rho\right)+C_{a,CF-RES}}} \qquad [1] \qquad (8)$$

$C_{a,CF-RES}$ value can be referred to the "Figure 2" below:

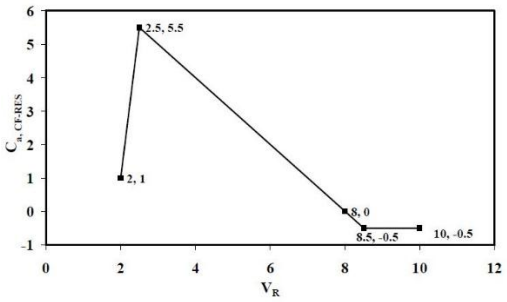

Figure 2: $C_{a,CF-RES}$ **as a function of reduced velocity [3]**

- Calculate the fatigue damage due to Cross-flow VIV at current flow velocity V_k (for K=1, 2, …, l*).

$$D_{fat\_cf\_k}\left(x_j\right)=f_{cyc,cf}\left(x_j\right).\left(\frac{S_{comb\_cf}\left(x_j\right).SCF}{MPa}\right)^{m\left(x_j\right)}.\frac{P_k}{\bar{a}\left(x_j\right)}\ [1] \qquad (9)$$

Where SCF is the stress concentration factor, P_k is the current flow probability at V_k by Weibull distribution. $m\left(x_j\right)$ is fatigue exponent by S-N curve and $\bar{a}\left(x_j\right)$ id characteristic fatigue strength constant.

- Calculate the Cross-flow VIV fatigue life:

$$D_{fat\_cf}\left(x_j\right)=\sum_{k=1}^{l^*} D_{fat\_cf\_k}\left(x_j\right)[1] \qquad (10)$$

$$D_{fat\_cf}=max\left(D_{fat\_cf}\left(x_j\right)\right)[1] \qquad (11)$$

for j=1,2,…,m*

$$T_{fat\_life\_cf}=\frac{\eta}{D_{fat\_cf}}[1] \qquad (12)$$

S-N Curve Theory for Multi-Span Fatigue Analysis

The S-N curve is a simple and efficient method for pipeline fatigue analysis, where the S-N data are usually determined by fatigue test. According to the latest version of DNV offshore structure steel structure code DNV-RP-C203, the basic design S-N curve is given as:

$$log\,N=log\,\bar{a}-m\,log\,\Delta\sigma\ [1]\text{-}[3] \qquad (13)$$

Where, N is the predicted number of cycles to failure for stress, $\Delta\sigma$ is the stress range, m is the negative inverse slope of S-N curve, $log\,\bar{a}$ is the intercept of the N-axis by S-N curve, it is given by the following formula:

$$log\,\bar{a}=log\,a-2s \qquad [1]\text{-}[3] \qquad (14)$$

Where a is the constant relating to mean S-N curve, s is the standard deviation of $log\,N$.

The fatigue life can be calculated based on the S-N curve under the assumption of linear cumulative damage by Palmgren-Miner and can be found from the following equation:

$$D_{fatLife}=\sum_{i=1}^{k}\frac{n_i}{N_i}=\frac{1}{a}\sum_{i=1}^{k} n_i\left(\Delta\sigma_i\right)^m \qquad [1]\text{-}[3] \qquad (15)$$

Where D_{fat} is the accumulated fatigue damage, $\bar{a}$ is the intercept of the design S-N curve with the log N axis, m is the negative inverse slope of the S-N curve, k is the number of stress blocks, n_i is the number of stress cycles in stress block i, N_i is the number of the cycles to failure at constant stress range $\Delta\sigma_i$.

Multi-Span Fatigue Analysis Case Study

Design Data

VIV fatigue analysis for multi-span pipeline with multi-mode response is performed for 32inch gas flow with 28/8mm wall thickness at water depth of 64m in Persian Gulf. Span design procedure is determined by allowable static and dynamic loads on free span. Then

on-bottom roughness analysis is performed to determine actual spanning condition. Free span length in this case study is considered about 20^{m} and L/D=24.6. This case study is a line pipe of 22^{th} phase of south pars gas field complex.

The design data in VIV fatigue analysis are present in "Table 1".

Table 1: Design Data for Multi-span fatigue analysis

Design Parameter	Unite	Value
Outer diameter of steel pipe	mm	812.8
Outer diameter of the pipe with coating	mm	862.8
Nominal wall thickness	mm	28.8
Pipeline model length	m	200
Pipe free span length L(m)	m	20
Water depth	m	64
Submerged weight at operation condition	N/m	1110.56
Current		Short term bottom current probability
Soil Type		Very soft Clay
Pipe Material		API-5L-X65
Steel Density	Kg/m^3	7850
Young's modulus	GPa	207
Specified Minimum Yield Strength(SMYS)	MPa	448
Specified Minimum Tensile Strength(SMTS)	MPa	535

The Environment Loads

The environment data must be collected for the long-term variation of the wave and current climate. For deep water pipeline fatigue analysis, the wave induced oscillatory flow can be negligible and only the steady flow due to current is considered in the analysis. In this regards, DNV-RP-F105 define a parameter named α which is ratio of velocity of current (U_c) to summation of velocity of current and velocity of current induced by significant wave amplitude (U_w).

$$\alpha = \frac{U_c}{U_c + U_w} \text{ [5],[6]} \qquad (16)$$

So in deep water effect of wave are negligible and only effect of current should be considered.

Current velocity is described by Weibull distribution which α, β and ϒ will be determine by Design Basis.

$$F_X(x) = 1 - exp\left(-\left(\frac{x-\gamma}{\alpha}\right)^{\beta}\right) \text{ [5],[6]} \qquad (17)$$

The current flow velocities varying from $0.5^{(m/sec)}$ to $0.7^{(m/sec)}$ have been considered for the pipeline fatigue life assessment. The probabilities of the current flow by Weibull distribution are present in "Figure 4".

Current reduced velocity and stability parameter are two parameters to control the vortex vibration resonance.

Analysis Results

Calculation of accumulated fatigue life of subsea pipelines is a complicated and long-time process. For the sake of the clarity, the procedure of calculation cumulative fatigue life is drawn in "Figure 5". The pipeline natural frequencies are summarized in "Table 2". The natural frequencies which shown in "Table 2" are the same output of ABAQUS software.

These data are based on the pipeline configuration for the operation load condition. For these natural frequencies, no significant VIV damage will occur in the present bottom current velocity range.

Refer to "Table 2", it is evident that the accumulated fatigue life is fairly significant for 25 years of design life.

It is well known that fatigue assessment due to multi-spanning in subsea pipelines are dependent to many factors such as soil-pipe interaction, pipeline residual laying tension, seabed properties, wall thickness of linepipes, environmental condition, etc. For determining the effect of any parameter in accumulated fatigue life time, it is essential to perform a sensitivity.

In this paper, accumulated fatigue life is calculated by consideration of the natural frequencies in constant span length-diameter ratio, and it is concluded that the effect of the first three natural frequencies in calculation of accumulated fatigue life are undeniable. As the natural frequency increases, its effect in calculation fatigue life is decreased and vice versa.

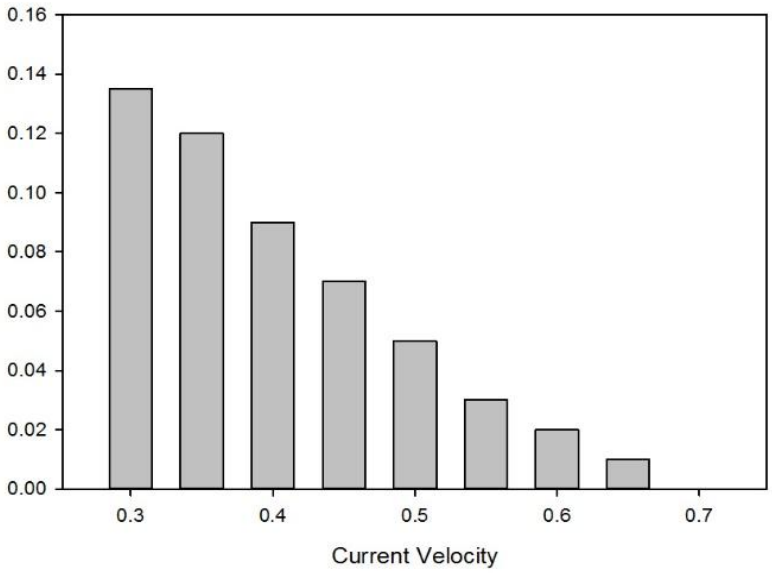

Figure 4: The current velocity probability by Weibull

Table 2: fatigue damage results for the design condition

Mode Number	Natural Frequencies(Hz)	VIV Fatigue Life	Design Fatigue Life
1	0.35	1768	25
2	0.93	1960	25
3	1.6	1972	25
4	2.1	1973	25

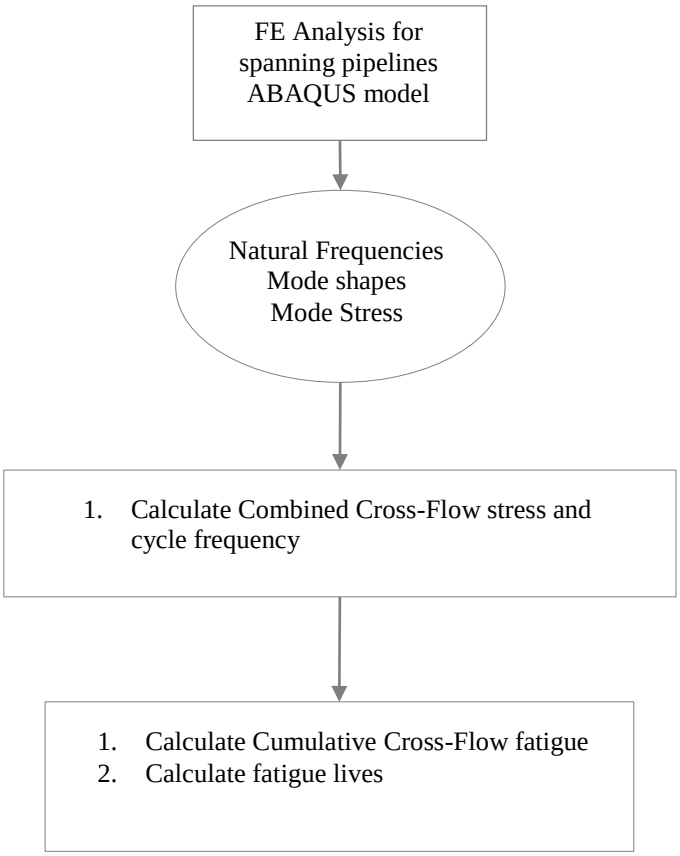

Figure 5. Flowchart to calculate fatigue life

Conclusion

The current paper refers to the effect of natural frequencies in fatigue assessment of Iranian south pars gas field due to multi-spanning. It is concluded that (table 2) that the first-three natural frequencies make 99.5% of cumulative fatigue life of pipe and others

make only 0.5% of that. Also it is concluded that the mode shapes with lower frequencies have more cooperation in fatigue life of a pipeline. Consideration of the first-three mode shapes of the pipeline is suitable and fairly good for calculation of cumulative fatigue life time due to multi-spanning in cross-flow direction. Also it can be observed that the rule (DNV-RP-F105) gives a pipe with an over design fatigue life.

List of Symbols

A_i	i^{th} mode cross-flow unit amplitude stress
$\left(A_Z/D\right)$	Normalized cross-flow VIV response
a	constant relating to mean S-N curve
$C_{a,CF-RES}$	added mass coefficient
D	Pipe outer diameter (include any coating layer)
D_{fat}	Deterministic fatigue damage
F(x)	cumulative fatigue damage
f_v	dominating vibration frequency
f_i	i^{th} eigen frequency of span cross-flow($f_{n,CF}$) natural frequency
f_{cyc}	Frequency used for fatigue stress cycle counting in case of multimode response
k	number of stress blocks for fatigue damage or number or flow velocity ranks
l^*	number of flow velocity rank
m	fatigue exponent or negative inverse slope of S-N curve
m^*	Number of ABAQUS pipeline mode node
m_e	effective mass per unit length
M	negative inverse slope of S-N curve
n^*	number of VIV modes
N	number of independent events in the return period
N_i	number of cycles to failure at constant stress range $\Delta\sigma_l$
n_i	number of stress cycles for i'th stress cycle
Pi	Probability of occurrence at flow velocity V_k by Weibull
$P_{Hs,T_p,\theta}$	Probability of occurrence of each individual sea-state
T_{life}	fatigue design life capacity
s	the standard deviation of LogN
Si	i'th stress range
t	pipe wall thickness or time
U_s	significant wave-induced flow velocity normal to the pipe, corrected for wave direction and spreading
U_c	current for wave direction and spreading
V_k	flow velocity at rank k
x_c	return period value
x_j	the axial location coordinate for the pipeline model at node j

Greek symbols

α	Weibull scale parameter
β	Weibull shape parameter and relative soil stiffness parameter
γ	Weibull location parameter
γ_s	safety factor on stress amplitude
$\gamma_{on,CF}$	safety factor on onset value for cross-flow
γ_f	safety factor on natural frequency
σ	stress, or standard deviation

References

[1] DNV-RP-F105 (2006), "Free Spanning Pipelines", Det Norske Veritas.

[2] DNV (2005), "Recommended Practive DNV-RP-C203 Fatigue Design of Offshore Steel Structures", Det Norske Veritas.

[3] DNV-OS-F101 (2007), "Submarine Pipeline Systems", Det Norske Veritas.

[4] Yong Bai and Qiang Bai (2005), "Subsea Pipelines & Risers", Chapter 10, "Vortex-induced Vibrations (VIV) and Fatigue".

[5] Bai, Y., & Bai, Q. (2014). Subsea Pipeline Integrity and Risk Management. Subsea Pipeline Integrity and Risk Management.

[6] k.rezazade, Y.Bai; Fatigue Analysis of Multi-Spanning Subsea Pipelines; 29th International Conference on Ocean, Offshore and Arctic Engineering OMAE2010 June 6-11, 2010, Shanghai, China

[7] Developments, S., & Industrial, W. (n.d.). Structural Integrity Monitoring.

[8] Mirzaei, M. (n.d.). Fracture Mechanics theory and application. Tarbiat Modarres University Publication.

[9] Veritas, D. N. (2011). Factory Applied External Pipeline Coatings for Corrosion Control, (May).

INTERNATIONAL JOURNAL OF
COASTAL & OFFSHORE ENGINEERING
IJCOE No. 3/Summer 2016 (19-26)

Pressure distribution around a near-wall circular cylinder subjected to steady current

M. A. Salehi[1],S. Mazaheri[2], M. H. Kazeminezhad[3]

[1] *Ocean Engineering and Technology Research Center, Iranian National Institute for Oceanography and Atmospheric Sciences, Tehran, Iran, mascivil9@gmail.com*
[2] *Ocean Engineering and Technology Research Center, Iranian National Institute for Oceanography and Atmospheric Sciences, Tehran, Iran, said.mazaheri@inio.ac.ir*
[3] *Ocean Engineering and Technology Research Center, Iranian National Institute for Oceanography and Atmospheric Sciences, Tehran, Iran, mkazeminezhad@inio.ac.ir*

ARTICLE INFO

Article History:
Received: 4 Jul. 2016
Accepted: 15 Sep. 2016

Keywords:
Circular cylinder
pressure distribution
force coefficient
separation angle
stagnation angle
vortex shedding

ABSTRACT

Flow around a circular cylinder near plane wall has been simulated using Open source CFD codes of OpenFOAM in different flow regimes (Re=100, 200, 3900) and different gap ratios (G/D= ∞, 1, 0.5, 0.2). Time-averaged pressure coefficients around a circular cylinder computed and compared with each others in different cases. Other features of flow including drag and lift coefficients, Strouhal number, separation angle and stagnation angle are also computed to describe the state of flow better. It has been shown that pressure distribution around the circular cylinder can be utilized to describe the variations in hydrodynamic force coefficients as well as other features of wake flow such as separation and vortex shedding phenomenon near a plane boundary. Plane wall effects on pressure distribution in different flow regimes investigated and it was found that the inception of vortex shedding suppression can be deduced from pressure distribution pattern, through pressure gradient between free-stream-side and wall-side of cylinder. In addition, a rapid increase in the maximum value of positive pressure coefficient can be concluded.

1. Introduction

Flow around circular cylinders near plane boundary has been a subject of interest for researchers because of its vast practical applications in ocean and offshore engineering such as offshore pipelines in various conditions particularly in free spans and near sea beds. Interaction between pipeline and fluid near a sedimentary seabed can promote erosion and free spans, which makes the pipeline vulnerable to vortex induced vibrations. Vortex shedding phenomenon leads to vortex induced vibration of a cylinder subjected to cross flow, which is undesirable due to fatigue concerns.

Measurements of the pressures and forces around a circular cylinder and their fluctuations can be used to describe the features of the interference between cylinder and plane and help control the occurrence of vortex shedding.

Zdravkovic, [1], categorized states of flow around a circular cylinder and its wake based on flow regimes and Reynolds number, according to Table 1.

Transition in Wake, Transition in Shear Layers and Transition in Boundary Layers, are shown in figure 2:

Table 1. States of flow around a circular cylinder in different flow regimes, [1]

State			Regime	Re changes
L	Laminar	1	No-Separation	0 to 4-5
		2	Closed Wake	4-5 to 30-48
		3	Periodic Wake	30-48 to 180-200
TrW	Transition in Wake	1	Far-Wake	180-200 to 220-250
		2	Near-Wake	220-250 to 350-400
TrSL	Transition in Shear Layers	1	Lower	350-48 to 1k-2k
		2	Intermediate	1k-2k to 20k-40k
		3	Upper	20k-40k to 100k-200k
TrBL	Transition in Boundary Layers	0	Pre-critical	100k-200k to 300k-340k
		1	Single Bubble	300k-340k to 380k-400k
		2	Two Bubble	380k-400k to 500k-1M
		3	Supercritical	500k-1M to 3.5M-6M
		4	Post-critical	3.5M-6M to ?
T	Fully Turbulent	1	Invariable	? to ∞
		2	Ultimate	

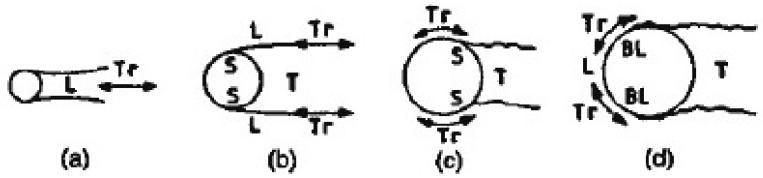

Figure 2- (a) Transition in Wake, (b) Transition in Shear Layers, (c),(d) Transition in Boundary Layers, [1]

First measurements of pressure distribution in laminar state of flow were carried out by Thom [2] in water and Homann [3] in oil. The single curve is drawn for the range $36 < Re < 107$ shows that there is negligible effect of Re on the base pressure, $C_{pb.}$ Thom, [2], and Homann, [3], measured mean pressure distribution around a circular cylinder in the TrW state of flow. There is a branching of curves beyond $\theta s = 70°$ and related variation in C_{pb}, where θs is the separation angle The separation angle θs can be estimated from the inflection in the curves to be in the range $95° < \theta s < 115°$. Note that higher values of θs correspond to lower Re and vice versa. Williamson and Roshko, [4], measured only the base pressure in the range $50 < Re < 350$ that covers the L3, TrWl and part of the TrW2 flow regimes. The laminar periodic regime, L3, shows a continuous increase in $-C_{pb}$ related to a decrease in L_f, the shortest length of eddy formation The first discontinuity at Re = 170 coincides with the appearance of fingers and the related drawing back of dye into the near-wake. Further shortening of Lf in TrWl leads to the increase in $-C_{pb}$ which leads at Re = 270, to $(-C_{pb})max$, and $(L_f)min$.

Bearman and Zdravkovic, [5], investigated flow around a circular cylinder at various heights above a plane boundary experimentally and found out flow around a circular cylinder near plane boundary depends on cylinder Reynolds number, gap ratio (G/D) and characteristics of the boundary layer. Distributions of mean pressure around the cylinder and along the plate were measured at a Reynolds number, based on cylinder diameter, of 4.5×10^5. Spectral analysis of hot-wire signals demonstrated that regular vortex shedding was suppressed for all gaps less than about 0.3 cylinder diameters and for gaps greater than 0.3 the Strouhal number was found to be remarkably constant. Zdravkovic, [6], measured the lift and drag forces on circular cylinders fitted with end plates in a wind tunnel. The gap between the cylinder and the wall, G, the thickness of the turbulent boundary layer along the wall, δ, and Re are varied in the following ranges: $0 < G/D < 2$, $12 < \delta/D < 0.97$ and $4.8 \times 10^4 < Re < 3 \times 10^5$. The lift and drag coefficients are presented in terms of a new variable G/δ. It was found that the lift coefficient is governed by the gap to diameter ratio *G/D* while the drag coefficient is dominated by the ratio of gap to thickness of the boundary layer, *G/δ.*

Pressure distribution around a cylinder near a plane boundary relates to displacement of stagnation point in front of cylinder toward gap and displacement of separation points around the cylinder. Since the flow structure around the separation point is the source of vortical instability in the wake, vortex shedding depends on the flow separation from the cylinder boundary layer.

Wu et al. ,[7], investigated The separation point of the flow around a circular cylinder numerically and experimentally in the regime of Reynolds number less than 280. It reveals that the variations of the time-averaged separation angles with Reynolds number can be represented by a simple linear θ_s–$Re^{-1/2}$ relationship for $10 < Re < 200$.

Some of near wall flow field parameters around circular cylinder have been illustrated in figure 1.

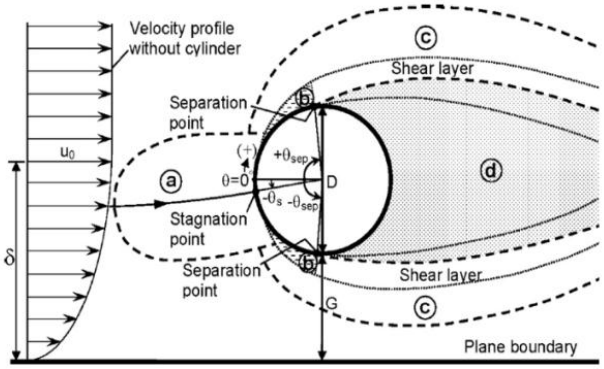

Figure 1. Definition of near wall flow field parameters around circular cylinder, [8]

According to above review, comparing pressure distribution around a circular cylinder near a plane boundary, in addition to provide information for hydrodynamic force computations, presents insight on near-wake characteristics of flow near plane boundary. In this study, pressure coefficient is defined as:

$$C_p = \frac{P - P_s}{\frac{1}{2}\rho U_\infty^2} \quad (1)$$

Where P is the pressure measured on the surface of the cylinder, P_s is the hydrostatic pressure taken from the cylinder position, ρ is the density of the water and U_∞ is the far field flow velocity.

In this study, three dimensional flow around a circular cylinder near plane wall has been simulated using Open source CFD codes of OpenFOAM in different flow regimes (Re=100, 200, 3900) and different gap ratios (G/D= ∞, 1, 0.5, 0.2).

Time-averaged pressure distribution around a circular cylinder presented graphically according to Gap ratio, G/D, and compared for Re=100,200 and 3900. The results show that the pressure distribution pattern can be used to describe near-wake flow around a circular cylinder, and the variation of flow configurations subjected to different geometrical and hydrodynamic situations.

Governing Equations:

Time averaged Navier-Stokes equations including continuity equation are the governing equations for incompressible fluid flow:

$$\frac{\partial u_i}{\partial x_i} = 0 \quad (2)$$

$$\rho\left(\frac{\partial u_i}{\partial t} + u_j \frac{\partial u_i}{\partial x_i}\right) = B_i - \frac{\partial p}{\partial x_i} + \mu \frac{\partial^2 u_i}{\partial x_j \partial x_j} + \frac{\partial}{\partial xj}\left(-\rho u_i' u_j'\right) \quad (3)$$

$$\tau = \left(-\rho u_i' u_j'\right) \quad (4)$$

Where u, p, ρ, υ, B and τ are the velocity, pressure, density, kinematics viscosity, body forces and Reynolds stress, respectively. K-ω SST, a two-equation eddy-viscosity turbulence model has been employed to close the system of equations. K-ω SST, presented by Menter (1994), is a variant of the standard k–ω model. Combines the original Wilcox k-w model for use near walls and the standard k–ε model away from walls using a blending function, and the eddy viscosity formulation is modified to account for the transport effects of the principle turbulent shear stress This turbulence model solves one transport equation for the turbulent kinetic energy, k, and one transport equation for the dissipation per unit kinetic energy, ω, also regarded as a turbulent frequency scale.

Computational Domain:

Computational domain of 30D×20D×10D dimensions with totally hexahedral meshes was created. Cylinder diameter "D" is set equal to 10cm. Boundary conditions for far field and near the plane wall cases are shown in Fig.2.

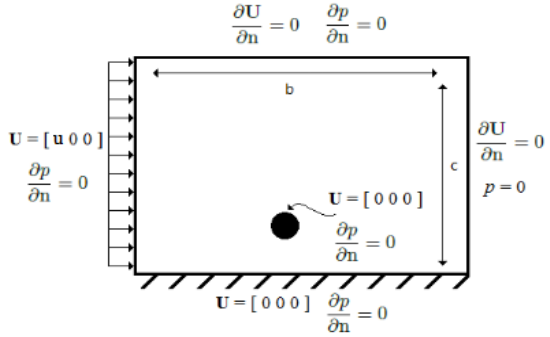

Figure 2. Boundary conditions for flow around circular cylinder near the wall

Numerical Model

IcoFoam, the basic laminar incompressible solver of OpenFOAM has been used for Re=100,200 while for Re=3900, PimpleFOAM (merged PISO-SIMPLE algorithm), which is a large time-step transient model has solver for incompressible flow alongside K-ω SST turbulence been employed to solve the equations.

Model Verification:

Comparison of simulation results for flow around circular cylinder far from plane boundary, including drag coefficient, positive maximum figure of lift coefficient and Strouhal number were considered and compared with those obtained by Cao and Wan, [9], Williamson, [10], Norberg, [11], and Rosetti et al, [12], showed good agreement, Table 1. Also the computational velocity fields from the present simulations are compared with the experimental results obtained from PIV measurements of Oner et al., [13], for further validation of the numerical code.

Table 2. Comparison of C_d, C_l(max) and S_t parameters for Re=100,200

	Re=100			Re=200		
	C_d	C_l	S_t	C_d	C_l	S_t
Present study	1.26	0.11	0.16	1.2	0.31	0.19
Cao and Wan	1.39	-	0.16	1.4	-	0.19
Williamson	-	-	0.16	-	-	0.19
Norberg	-	0.12	0.16	-	0.32	0.18
Rosetti et al.	1.41	-	0.17	1.3	-	0.2

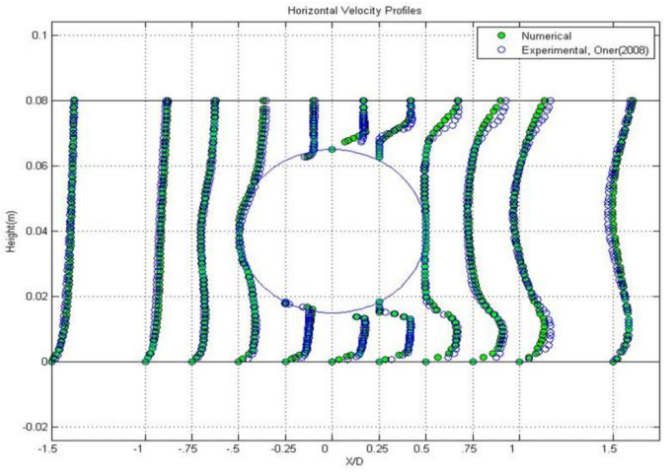

Figure 3.comparison of horizontal velocity profiles of present numerical simulation and experimental study of Oner et. al, [13] for G/D=0.3 and Re=9500

Results and Discussion

Tables 2,3 and 4 present the results of 3-D computations including hydrodynamic drag, cd(mean) and lift coefficients, cl(rms), Strouhal number (st), gap to boundary layer thickness ratio (G/δ), Separation angle, Stagnation angle and base pressure, Cpb, for different gap ratios and Re=100, 200 and 3900. It has been observed that for the range of $G/\delta < 0.45$ there is a high possibility of vortex shedding suppression. The thickness of the boundary layer, δ, can be determined by measuring the velocity profile of the boundary layer at the cylinder location.

Table 2: 3-D numerical results of flow around circular cylinder far from and near the wall for Re=100

Re=100	G/D= ∞	G/D=1	G/D=0.5	G/D=0.2
cd(mean)	1.269	1.61	1.405	1.165
cl(rms)	0.111	0.2	0.163	0.598
st	0.161	0.183	0.092*	0.196*
G/δ	-	1.042	0.521	0.208
separation angle	114.72	98.97	95.51	92.29
stagnation angle	0	-2.2	-5.5	-9
Cpb	-0.53	-0.64	-0.52	-0.56

Table 3: 3-D numerical results of flow around circular cylinder far from and near the wall for Re=200

Re=200	G/D= ∞	G/D=1	G/D=0.5	G/D=0.2
cd(mean)	1.208	1.518	1.425	1.143
cl(rms)	0.306	0.492	0.342	0.417
st	0.192	0.209	0.1	0.25*
G/δ	-	1.19	0.595	0.238
separation angle	108.07	98.97	95.51	92.29
stagnation angle	0	-2.2	-8.1	-11
Cpb	-0.69	-0.86	-0.72	-0.57

Table 4: 3-D numerical results of flow around circular cylinder far from and near the wall for Re=3900

Re=3900	G/D= ∞	G/D=1	G/D=0.5	G/D=0.2
cd(mean)	1.281	1.712	1.544	1.238
cl(rms)	0.677	1.032	0.896	0.51
st	0.214	0.18	0.092	0.04*
G/δ	-	2.174	1.087	0.435
separation angle	98.98	98.97	92.75	85.5
stagnation angle	0	-2.2	-14.7	-6.8
Cpb	-1.15	-1.71	-1.13	-0.91

Time-averaged pressure distribution around a circular cylinder and separation points for all cases, cylinder far from and near the wall, have been presented in figures 4, 5 ,7 and 8. Pressure distribution has been represented by pressure coefficient, C_p. Pressure distribution pattern around a circular cylinder with gap ratio of G/D=1 in current study is similar to Bearman and Zdravkovic study, [5] , for G/D=1 and different Reynolds number, Figures 5 and 6.

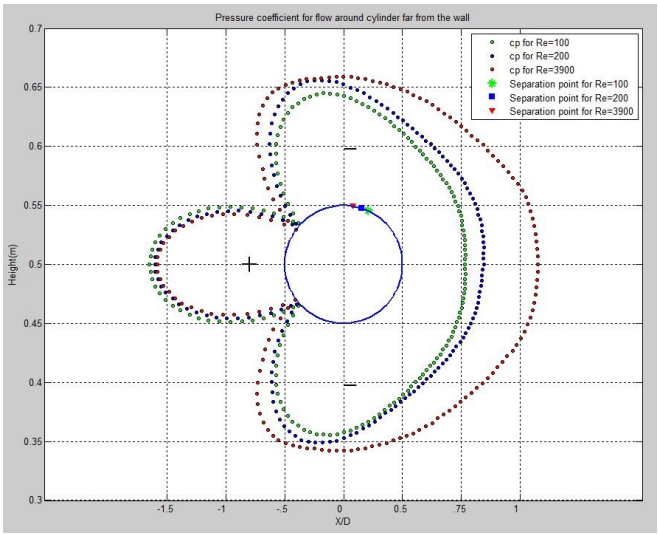

Figure 4. Pressure coefficient distribution around circular cylinder at G/D=∞, for Re=100,200,3900

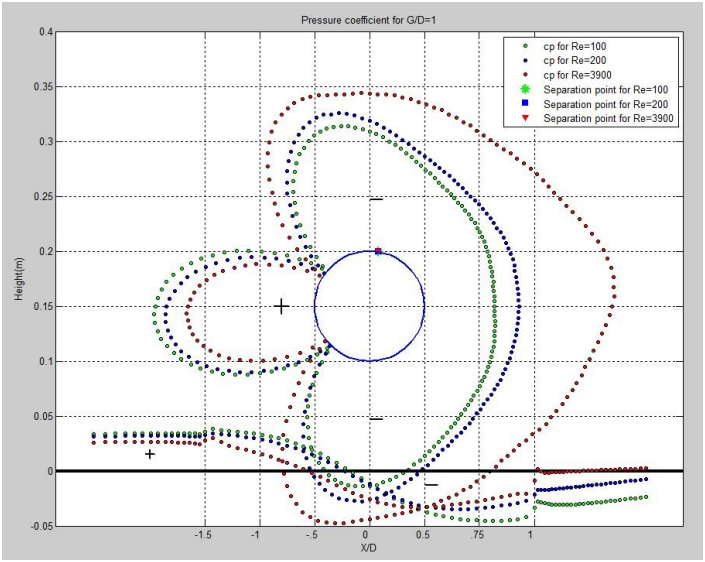

Figure 5. Pressure coefficient distribution around circular cylinder at G/D=1, for Re=100,200,3900

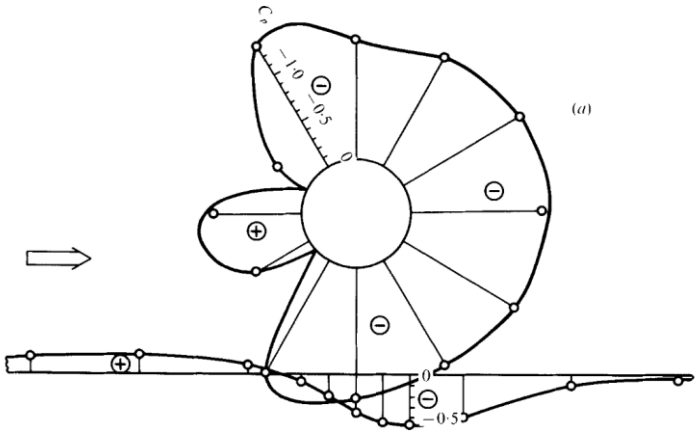

Figure 6. Pressure coefficient distribution around circular cylinder at G/D=0.1, for Re=4.5×10^4, [5]

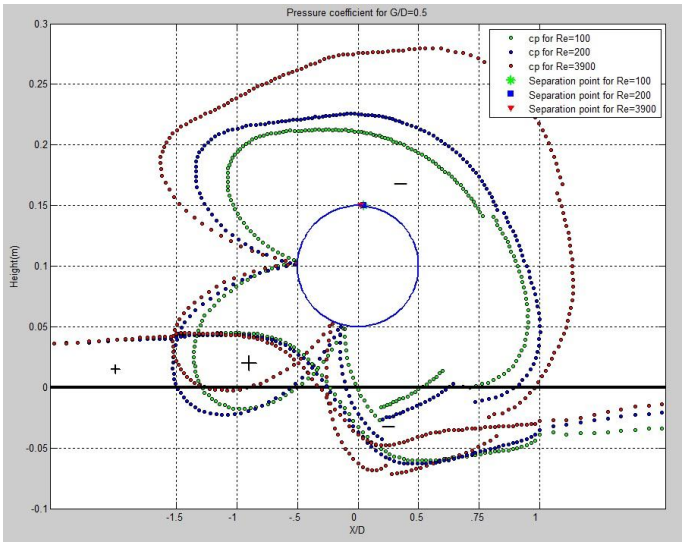

Figure 7. Pressure coefficient distribution around circular cylinder at G/D=0.5, for Re=100,200,3900

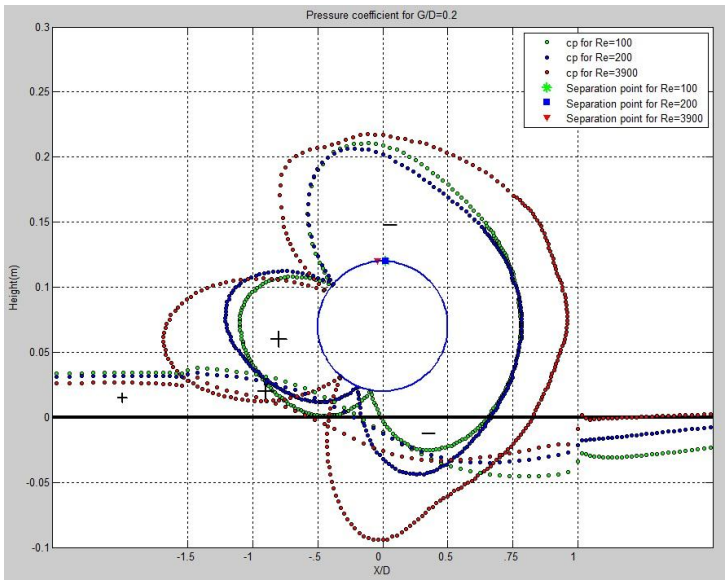

Figure 8. Pressure coefficient distribution around circular cylinder at G/D=0.2, for Re=100,200,3900

It is seen that bell-shaped pressure coefficient distribution pattern includes a smaller section of positive pressure coefficient in front of cylinder and a bigger section of negative pressure coefficient around the other parts of the cylinder perimeter. In all cases, far from and near the wall, the symmetry of pressure coefficient around the stagnation point has been observed. Investigation of pressure coefficient around the cylinder shows that by reducing gap ratio, G/D, higher lift force pushes the cylinder upward. The

amount of lift increase is less pronounced when vortex shedding suppressed or boundary layer is thicker. By increasing G/D, positive and negative values of pressure coefficients around the cylinder decreased, hence mean lift force on the cylinder decreases too. In high inference between the cylinder and the wall, i.e. smaller G/D, and when boundary layers around the cylinder and the wall overlap more fittingly, the maximum of positive pressure coefficient increases and moves downstream.

Vortex shedding suppression can be predicted by monitoring the variations of pressure distribution around the circular cylinder near the boundary, hence suppression can be preceded by modifying the pressure distribution patterns. Vortex shedding suppression observed in 4 cases, all of three cases of flow around a circular cylinder near wall with G/D=0.2 and the other one for flow around a circular cylinder near wall with G/D=0.5 and Re=100. For these cases, a sustained negative pressure is observed at the free-stream side of the cylinder and a less pronounced negative pressure is observed at the wall-side of the cylinder. The maximum of positive pressure coefficient experiences a chamber in shape and a bit of decrease in value while suppression occurs. Insufficient gradient of pressure between free-stream side and wall-side of cylinder leads to a static and stable state of shear layers, which prevents the process of vortex shedding to proceed or in intense condition, i.e. very low G/δ, shear layers don't even manage to roll-up. Time-averaged streamlines around a circular cylinder for G/D=0.2 and Re=100 demonstrates the latter description, figure 9.

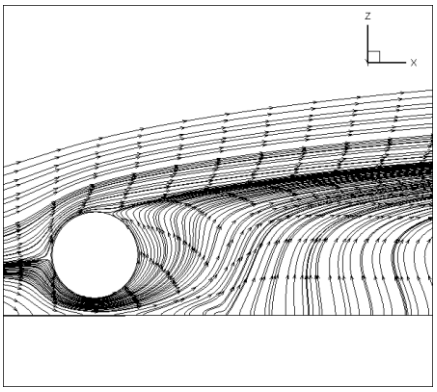

Figure 9. Time-averaged streamlines for flow around a circular cylinder for G/D=0.2 and Re=100

Based on figures 4, 5 ,7 and 8, it can be observed that upper separation point moves counter-clockwise by increasing Reynolds number (decrease in separation angle, θ_s), in a fixed gap ratio. Also in a fixed Reynolds number, upper separation point moves upward by decreasing G/D (decrease in separation angle, θ_s). Upward displacement of upper separation point by approaching the wall ,can be described by the growing stream-wise pressure gradient induced by the gap flow. Separation occurs when skin friction vanishes, where velocity gradient at the wall becomes zero. The effect of the boundary layer on the pressure distribution can be attributed to the existence of the velocity gradient in the boundary layer. Drag coefficient consists of friction drag and form (pressure) drag and major fluctuations of drag force around circular cylinder relates to form drag in a distinct flow regime. When drag coefficient, a function of pressure distribution, rapidly decreases, it can be deduced that friction drag increases with respect to form drag and velocity gradient reaches its maximum value, hence separation of boundary layer does not proceed, i.e. vortex shedding suppression occurs.

Stagnation point is the correspondent point on the cylinder surface to the maximum of positive pressure coefficient. It is shown that stagnation point moves toward wall by increasing Reynolds number (decrease in stagnation angle).

According to tables 2, 3 and 4, Mean drag coefficient, Cd(mean) generally increases with increasing Gap ratio, G/D. But from G/D=1 to G/D=∞, considering the ratio of gap distance to cylinder boundary layer thickness, G/δ, reduce in drag coefficient observed, which is the result of the cylinder exit from the influence zone of plane wall`s boundary layer. Oscillating lift coefficient, represented by Cl(rms), root mean square of lift coefficient, in Re=100, where boundary layer is thicker, shows bigger value near the wall, while for Re=3900, where boundary layer is thinner. Increase of Cl(rms) near the wall in thick boundary layer can be explained by increase of the lift coefficient near the wall, as a result of the perturbance of reverse pressure gradient above and below the cylinder which makes the positive fluctuations of lift coefficient bigger.

vortex shedding frequency, represented by Strouhal number, St, in thicker boundary layers (lower Reynolds numbers) increases by decreasing G/D and vice versa.

Summary and conclusions

Flow around a circular cylinder near plane has been studied in different flow regimes (Re=100, 200, 3900) with different gap ratios (G/D=∞, 1, 0.5, 0.2). Pressure distribution around the circular cylinder has been utilized to describe the variations in hydrodynamic force coefficients as well as other features of wake flow such as separation and vortex shedding phenomenon near a plane boundary. Plane wall effect on pressure distribution in different flow regimes was also assessed. it was found out that the inception of vortex shedding suppression can be deduced from pressure distribution pattern, through pressure gradient between free-stream-side and wall-side of cylinder and also the sudden decrease in maximum of positive pressure coefficient. Mean drag coefficient increases when cylinder approaches the

wall until G/D=1, but when cylinder submerges further in the plane wall's boundary layer, Cd(mean) decreases as C_{pb} decreases. Cl(rms) near the wall in thick boundary layer near the wall, increases as a result of the perturbance of reverse pressure gradient above and below the cylinder which makes the positive fluctuations of lift coefficient bigger. In a constant flow regime, upper separation point moves upward by decreasing G/D, indicates that the separation angle, θ_s decreases too. this can be described by the growing stream-wise pressure gradient induced by the gap flow.

References

[1] Zdravkovich, M. M., Flow Around Circular Cylinders, Vol 1: Fundamentals. Oxford University Press Inc, 1997.

[2] Thorn, A., "The flow past circular cylinders at low speeds". *Proceedings Royal Society*, A141, 651-69, 1933J.

[3] Homann, F., "Influence of higher viscosity on flow around cylinder" (in German). Forschung aus *dem Gebiete* des *Ingenieiuwesen*, **17,** 1-10, transl, 1952. NACA TM 1334., 1936J.

[4] Williamson, C. H. K., and Roshko, A. (1990J). Measurements of base pressure in the wake of a cylinder at low Reynolds numbers. *Zeitschriit fur Flugwissenscbeiten und Weltraumorsdwng*, 14,38-46. (Exp. 50 <*Re* < 290, *St*, FV, PS). 3, 1990J.

[5] Bearman P.W. & Zdravkovich M.M., "Flow around a circular cylinder near a plane surface", *Journal of Fluid Mechanics*, Vol. 89, pp. 33-47, 1978.

[6] Zdravkovich M.M., "Forces on a circular cylinder near a plane wall", *Applied Ocean Research.*,Vol.7, pp.197-201, 1985.

[7] Wu, M. H., Wen, C. Y., Yen, R. H., Weng, M. C., Wang, A. B., "Experimental and numerical study of the separation angle for flow around a circular cylinder at low Reynolds number", *Journal of Fluid Mechanics*, vol. 515, pp.233-260, 2004.

[8] Kirkgoz, M. S., Oner, A. A. and Akoz, M. S. , "Numerical Modeling of Interaction of a Current with a Circular Cylinder near a Rigid Bed". *Advances in Engineering Software*, 40, 1191-1199, 2009.

[9] Cao, H., Wan, D., "Application of OpenFOAM to Simulate Three-Dimensional Flows past a Single and Two Tandem Circular Cylinders" , Proceedings of the Twentieth (2010) International Offshore and Polar Engineering Conference Beijing, China, June 20-25, 2010.

[10] Williamson, C. H. K. (1991). "2-D and 3-D Aspects of the Wake of a Cylinder, and Their Relation to Wake Computations", *Lect Appl Math*, Vol 28, pp 719-751, 1991.

[11] Norberg, C., (2003), "Fluctuating lift on a circular cylinder: review and new measurements, *Journal of Fluids and Structures"* 17, 57–96, 2003.

[12] Rosetti, G. F., Vaz, G. and Fujarra, A. L. C.,(2012), "URANS Calculations For Smooth Circular Cylinder Flow In A Wide Range Of Reynolds Numbers: Solution Verification And Validation", *Journal of Fluids Engineering*, Vol. 134, 121103, 2012.

[13] Oner, A.A., Kirkgoz, M.S., Akoz, S., "Interaction of a current with a circular cylinder near a rigid bed", *Journal of Ocean Engineering*, Vol. 35, 1492-1504 , 2008.

INTERNATIONAL JOURNAL OF
COASTAL & OFFSHORE ENGINEERING
IJCOE No. 3/Summer 2016 (27-33)

Speed Control of Autonomous Underwater Vehicle with Constraints Using Model Predictive Control

Seyyed Hossein Ghenaati [1], Shahram Aghaei [2]*

[1]*Electrical and Computer Department, Yazd University, Yazd, Iran; ghenaati@stu.yazd.ac.ir*
[2]*Assistant Professor, Electrical and Computer Department, Yazd University, Yazd, Iran; aghaei@yazd.ac.ir*

ARTICLE INFO

Article History:
Received: 8 Feb. 2016
Accepted: 15 Sep. 2016

Keywords:
Autonomous Underwater Vehicle
Model Predictive Control
Optimization
Constraint Satisfaction

ABSTRACT

Nowadays Autonomous Underwater Vehicles (AUVs) are an unavoidable part of marine industries. One of the most important parts of any autonomous vehicle is the control issue to achieve the desired performance. This paper is concerned with speed control of an AUV model respecting the state and control constraints. According to the Newton-Euler method, the 6 DOF kinematic and dynamic models of the AUV are established. A well-defined performance index and constrained finite horizon optimization program in the form of Model Predictive Control (MPC) strategy is proposed to regulate the horizontal speed of AUV to its desired value while the constraints on the states like depth and control signals are considered in finite time horizon optimization program to be satisfied. The main problem for such a situation is the interaction between speed control and depth deviation then quadratic programing technique managed responses to avoid state and control signal constraints. Simulation results show a reliable performance of proposed MPC strategy to control the horizontal speed of AUV while all the constraints on state, control signal and also the variation of the control signal are satisfied.

1. Introduction

Autonomous Underwater Robotic Vehicles have become an important tool to explore the secret life undersea. Then researches on AUV systems have been important since two decades and deals with wide variety of fields such as research, inspection, recovery, construction, rescue maneuvering and etc. [1-3]. The first commercial use of underwater vehicles commenced with the discovery of offshore oil and gas fields in North Sea then due to required complex maneuvering, autonomous type of underwater vehicle is becoming more popular as regards it can operate and explore in extreme depth especially is useful for offshore industries.

Nonlinear dynamic AUV model is introduced in several references [4-7]. Many scientists have focused on control, stability analysis and optimization concepts. Valentinis *et al*. [8] used energy based control design strategy and designed feedback control based on port Hamilton theory of motion control. Yushida *et al*. [9] implemented two air cored electromagnets to maintain the pitching stability. Elnashr [10] used phase plane analysis to study stability of AUV for two main decoupled systems of depth and heading control. Bagnia *et al*. [11] applied MPC on AUV depth control. Fernandez [12] presented an MPC approach to reducing under water robot position error under the influence of water waves performed in two-dimensional coordination. Johansen *et al*. [13] developed a collision avoidance system using MPC algorithm. Zhao *et al.* [14] introduced a new approach to real time collision avoidance that complies with COLREGS rules for underwater surface vehicle. Akçakaya *et al.* [15] designed a real time MPC schedule for set tracking control of variable speed AUV. Franze and lucia [16-17] described discrete time linear time invariant (LTI) model and applied receding horizon control strategy to solve obstacle avoidance motion planning algorithm.

In this paper, a well-defined performance index along with a constrained finite horizon optimization program propose an MPC strategy to regulate the horizontal speed of AUV to its desired value while the constraints on the states and control signals are considered in finite time horizon optimization program to be satisfied. The benefit of this work is about analysis of whole model of AUV and lack of necessity for decoupled model brings about all undesirable motions to be considered as feasible constraints therefore this process decreases interactions. In order to reduce modeling error, we

linearized system in every discretization step time frequently. The obtained results show that applied MPC strategy on the linearized model of AUV can control the system such a manner that all states achieve desired steady state values while initial states have unfavorable values. The simulation results of the above mentioned idea are presented in this paper while some conditions and properties of the idea such as designing proper terminal constraint and terminal set leading to stability and feasibility are left to next papers, when the research to be completed.

This paper has been organized as follows: In the following section, a discussion on modeling the AUV together with constraint structure for speed control program is presented. The next two sections provide details of the proposed MPC scheme and simulation results, respectively. The final section concludes the presented work.

2-Kinematic and dynamic modeling and requisite constraints

As shown in "Figure 1", AUV contains sail plane in addition to rudder and elevator planes to comprehensive navigation and main propeller motor motivates vehicle and "Figure 2" represents global and body fixed coordinate with OXYZ and oxyz respectively.

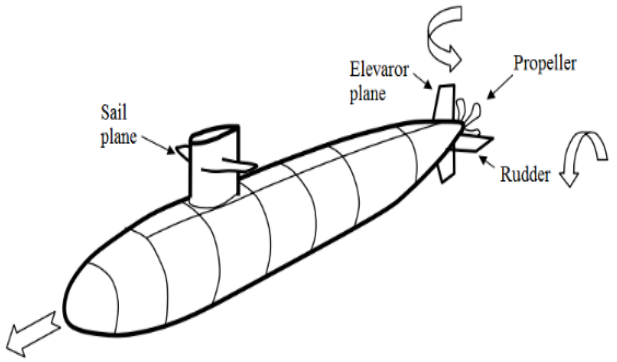

Figure 1: Submarine body and actuators [7]

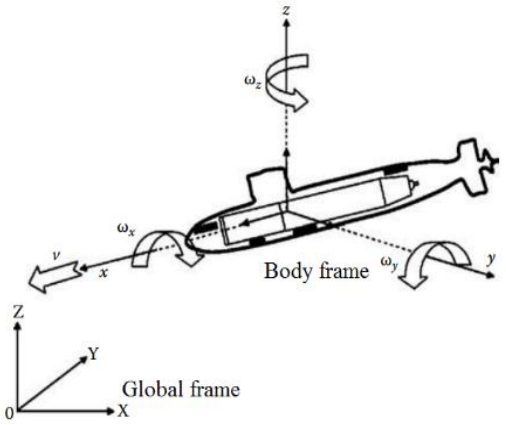

Figure 2: Body frame and Global frame illustration [7]

According to charted parameters in the "Table 1", 12 nonlinear states contain locations and Euler angles in global frame besides linear and angular velocities from body frame in the form of position and velocity vectors are defined as follows: $n_1 = (x\ y\ z)^T$, $n_2 = (\varphi.\theta.\psi)^T$, $n = (n_1.n_2)^T$, $V = (u.v.w)^T$, $\omega = (p.q.r)^T$, $v = (V.\omega)^T$ then effective force and torque vectors are defined as: $\tau_1 = (Fx.Fy.Fz)^T$, $\tau_2 = (Mx.My.Mz)^T$, $\tau = (\tau_1\ \tau_2)^T$ and the center of gravity is $r_G = (x_G.y_G.z_G)^T$. Transformation of position and velocity vectors from body frame to global coordinate is calculated with the following formulation where J is known as coordinate transformation matrix. There are two coordination transform matrices to calculate nonlinear state velocity of positions and angles in global frame therefore equations (1)-(2) depict coordinate transform matrices and equation (3) calculates nonlinear state velocities, based on coordinate transformation matrix. Surge, sway and lift velocities explain first order derivation of vehicle motions and derivation of Euler angles is depending on coordinate transformation matrix and angular velocities in body fixed frame.

$$J_1(n_2) = \begin{pmatrix} \cos\theta\cos\psi & -\sin\psi\cos\varphi+\cos\psi\sin\theta\sin\varphi & \sin\psi\sin\varphi+\cos\psi\cos\varphi\sin\theta \\ \sin\psi\cos\theta & \cos\psi\cos\varphi+\sin\varphi\sin\theta\sin\psi & -\cos\psi\sin\varphi+\sin\theta\sin\psi\cos\varphi \\ -\sin\theta & \cos\theta\sin\varphi & \cos\theta\cos\varphi \end{pmatrix} \quad (1)$$

$$J_2(n_2) = \begin{pmatrix} 1 & \sin\varphi\tan\theta & \cos\varphi\tan\theta \\ 0 & \cos\varphi & -\sin\varphi \\ 0 & \cos\varphi\sec\theta & \sec\theta\cos\varphi \end{pmatrix} \quad (2)$$

$$\begin{cases} \dot{n_1} = J_1(n_2)\ V \\ \dot{n_2} = J_2(n_2)\ \omega \end{cases} \quad (3)$$

Table 1: Motion modes, states and effective forces of AUV

Degree of freedom	Motion modes	Force/Torque (in the body frame coordinate)	Linear Velocity/angular Velocity (in the body frame coordinate)	Location/Euler angles (in the global frame coordinate)
1	Surge	F_x	u	x
2	Sway	F_y	v	y
3	Lift	F_z	w	z
4	Roll	M_x	p	φ
5	Pitch	M_y	q	θ
6	Yaw	M_z	r	ψ

We discussed vehicle kinematic relationship between body and global frames before and so as to dynamic model. Based on Euler-Newton theorem which describes Euler two laws of motion [18], we wrote the rigid body dynamic equations in six degrees of freedom in equations (4)-(9). All forces and torques in the right section of equations (4)-(9) definitely are produced by propeller speed and plane deflections as well as hydrodynamic forces constructed from fluid inertia force, fluid viscous force and restoring force. Brief of constructions and influence of mentioned forces are given in reference [19]. Equations (4)-(6) explain dynamic behavior of body forces and derivation of linear and angular velocities while body torque affluence affects dynamic model in equations (7)-(9).

As mentioned before MPC optimization process considers constraints inclusive signal bounds and interactions then this ability together with prediction increases robustness, applicability and softness for outputs and actuators. Regarding to singularity, stability and operational issues, "Table 2" charted all requisite constraints to solve this problem.

$$m[\dot{u} - vr + wq - x_G(q^2 + r^2) + y_G(pq - \dot{r}) + z_G(pr + \dot{q})] = F_x \quad (4)$$
$$m[\dot{v} - wq + ur + x_G(qp + \dot{r}) - y_G(p^2 + r^2) + z_G(qr - \dot{p})] = F_y \quad (5)$$
$$m[\dot{w} - uq + vp + x_G(rp - \dot{q}) + y_G(rq + \dot{p}) + z_G(p^2 + q^2)] = F_z \quad (6)$$
$$I_x\dot{p} + (I_z - I_y)qr + m[y_G(\dot{w} + vp - uq) - z_G(\dot{v} + ur - wq)] = M_x \quad (7)$$
$$I_y\dot{q} + (I_x - I_z)rp + m[z_G(\dot{u} + wq - vr) - x_G(\dot{w} + vp - uq)] = M_y \quad (8)$$
$$I_z\dot{r} + (I_y - I_x)pq + m[x_G(\dot{v} + ur - wp) - y_G(\dot{u} + wq - vr)] = M_z \quad (9)$$

Table 2. State and actuator constraints

Rudder angle (low limit)	-30°	Rudder angle variation per second (low limit)	-4°
Rudder angle (high limit)	+30°	Rudder angle variation per second (high limit)	+4°
Propeller speed (low limit)	0 RPM	Propeller speed variation per second (low limit)	-40 RPM
Propeller speed (high limit)	1800 RPM	Propeller speed variation per second (high limit)	+40 RPM
Pitch angle (low limit)	-30°	Pitch angle (high limit)	+30°
Depth interaction	11		

3. MPC scheme for speed control

MPC is an optimizing method which predict future behavior of known LTI models by discrete time slots and assumes discrete constrained control signals such a predictive way that a performance index with weighted coefficients reflecting to relative importance of states and control signals, can be reduced. The main advantage of MPC is the fact that this strategy allows the current time slot to be optimized while keeping future timeslots in account. This approach considers optimizing a finite time horizon but just implementing the current timeslot and due to quadratic programing method, MPC has capability of produce instant feasible trajectories respected to various kind of input and output restrictions. Extending of MPC in industrial problems is extremely appealing thanks to these inherent features which makes smooth response in actuators.

The design of speed control in the right direction is of interest both from the view of motion stabilization as well as tracking performance. We linearized then discretized system at certain operating point then MPC according to quadratic programing method [20] tries to find optimized control signals for prediction horizons based on linearized model. Defined effective weighted coefficients in performance index makes all motions and rotations nearby zero except surge velocity in other word output control signals hold non desired motions to zero. Due to regulate velocity just in x direction hence horizontal direction and improve

quadratic programing schedule we just consider propeller speed and rudder deflection in account then prevent stern and elevator from deflection while speed control scheme.

Applying tools from linear system theory fundamentally needs transformation of nonlinear system to linearized form so that be approximately equal to original system therefore MPC requires a linear discrete time model for optimizing process. Linearization and discretizing operations will be applied every 250 milliseconds as discretizing moment alternatively due mainly to decrease the modeling error inasmuch as variation of actual model in different positions. Regarding to this fact very high number of Np causes infeasible and wrong responses. Neglecting the disturbance and ocean current, equation (10) illustrates AUV model in state space form.

$$\begin{cases} \dot{x} = f(x,u) \\ y = h(x) \end{cases} \tag{10}$$

Where comprehensive description of $f(.)$ exists in previous section and $h(.)$ possesses all states separately. We can achieve linear approximation as equation (11) whereas high order derivations of basic model in Taylor series expansion is omitted.

$$\begin{cases} \dot{\tilde{x}} = \frac{\partial f}{\partial x}|_0 \, \tilde{x} + \frac{\partial f}{\partial u}|_0 \, \tilde{u} = A\,\tilde{x} + B\,\tilde{u} \\ \dot{\tilde{y}} = \frac{\partial h}{\partial x}|_0 \, \tilde{x} = C\,\tilde{x} \end{cases} \tag{11}$$

Where $(\tilde{x}, \tilde{u}, \tilde{y})$ denote deviation of states and outputs and subscript 0 means Jacobean matrices is evaluated at the operating point. Equation (12) describes conversion from continuous to discrete time version and equation (13) approximates linear discrete time model for MPC optimization procedure as Δt is discretization step size.

$$\begin{cases} F = e^{A\,\Delta t} \\ G = e^{A\,\Delta t} \int_0^{\Delta t} e^{-A\,\Delta\tau}\, d\tau\, B \end{cases} \tag{12}$$

$$\begin{cases} x(k+1) = F\,x(k) + G\,u(k) \\ y(k+1) = C\,x(k) \end{cases} \tag{13}$$

Equation (14) summarizes state prediction where state vector X contains states of Np timeslots with relative control horizon variations. X_0, X_M and U_{-1} are initial and desired states and previous control signals respectively and length of ΔU which calculates control signal variations is considered as long as prediction horizon.

$$\begin{pmatrix} X_1 \\ X_2 \\ \vdots \\ X_{Np} \end{pmatrix} = \begin{pmatrix} F \\ F^2 \\ \vdots \\ F^{Np} \end{pmatrix} X_0 + \begin{pmatrix} G & 0 & \cdots & 0 \\ GF^1 & G & \cdots & 0 \\ \vdots & \vdots & \ddots & \vdots \\ GF^{Np-1} & GF^{Np-2} & \cdots & G \end{pmatrix} \left\{ \begin{pmatrix} U_{-1} \\ U_{-1} \\ \vdots \\ U_{-1} \end{pmatrix} + \begin{pmatrix} I & 0 & \cdots & 0 \\ I & I & \cdots & 0 \\ \vdots & \vdots & \ddots & \vdots \\ I & I & \cdots & I \end{pmatrix} \begin{pmatrix} \Delta U_0 \\ \Delta U_1 \\ \vdots \\ \Delta U_{Np-1} \end{pmatrix} \right\} \tag{14}$$

After definition of prediction behavior of model based on states and control signal variations in Np timeslots, the performance index includes state difference from desired values and control signal variation as equation (15).

$$PI = \sum_{i=0}^{Np-1} (X_i - X_M)^T\, Q\, (X_i - X_M) + (\Delta U_i)^T\, R\, (\Delta U_i) + (X_{Np} - X_M)^T\, P\, (X_{Np} - X_M) \tag{15}$$

Then quadratic programing method described in reference [20] optimizes well-defined performance index in equation (15) regarding to restrictions and Q = [400,100,10,1,400,500] is relevant weighting state gain, R = [0.1 0.01] is responding control gain and P describes terminal constraint coefficients for optimizing speed control solution. Both equation (15) and mentioned constraints for speed control scheme in "Table 2", consist a finite horizon optimal control program that means we defined a MPC structure for horizontal speed control of AUV. Complete knowledge about steady state value of states (X_M) is necessary to achieve desired performance and initial state situation may have effects too. Regarding to our problem and initial situation, steady state vector of 12 states is defined as X_M = [200,0,10,1,0,0,0,0,0,0,0,0] which describes final behavior of AUV. MPC executes optimization process to decrease error between actual state values and desired ones. The last section of equation (15) is terminal state constraint to achieve infinite horizon control that guarantees closed-loop stability and P as terminal weight is calculated in such a way that optimal value of performance index roles as a Lyapunov function [20-22]. The other objective which is necessary to investigate for respecting the feasibility issue of on-line optimization is constructing a terminal constraint. Research about this issue and achieving a powerful formulation to calculate the proper terminal set -as considered [21-23] and references in there- corresponding to local linearized model or original nonlinear system is in hand and will be reported in next papers.

4. Results and Discussion

Some states like Y and φ are absolutely invariant since not only drag force and ocean current are

neglected but also rigid body and symmetric design assumption in addition to zero initial states and zero elevator angle are considered. Whereas some deviations exist in practice while ignoring presumptions. Speed regulation at $1\,m/s$ in x direction is demanded and "Figure 3" illustrates speed control and "Figure 4" depicts pitch angle solution with different number of prediction horizon.

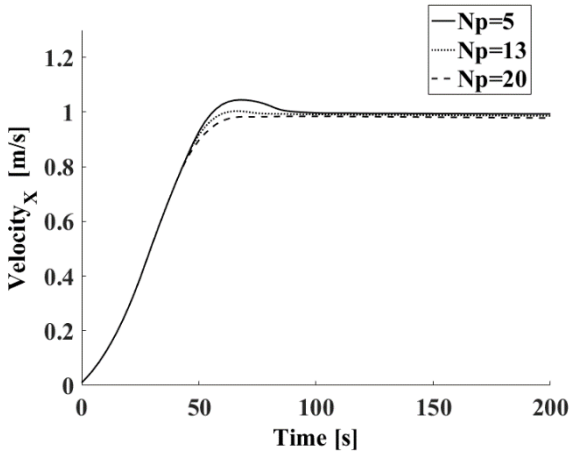

Figure 3: Speed regulation with different number of prediction horizon

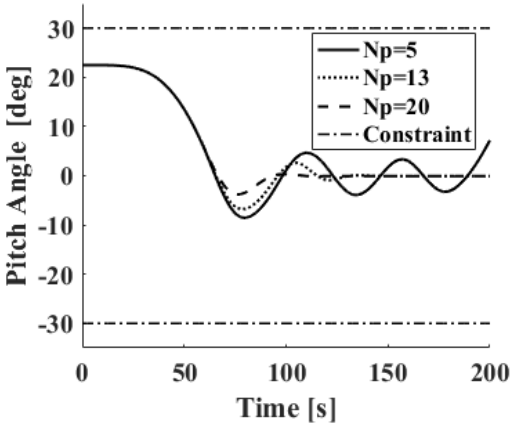

Figure 4: Pitch angle stabilization with different number of prediction horizon

A low quantity of prediction horizon makes uneven signals and increases tracking error but in other hand high quantity for prediction horizon may have ruined speed regulation respected to wrong estimation based on instant linearized model. Whereas vehicle achieve desired linear velocity, pitch angle must vary how much that decreases motion interactions on sway and lift directions as much as possible so pith, yaw and roll angles are expected to reach zero. If body frame matches global coordinate frame, vehicle linear velocity motivates just in x direction of vertical plane and coordinate transformation matrix must be identity. In order to satisfy favorites and respected to all restrictions, MPC moves pitch angle from initial value to zero and accelerates vehicle till desired speed concurrently. Rudder deflection and propeller motor speed as control signals is depicted in "Figure 5"and "Figure 6".

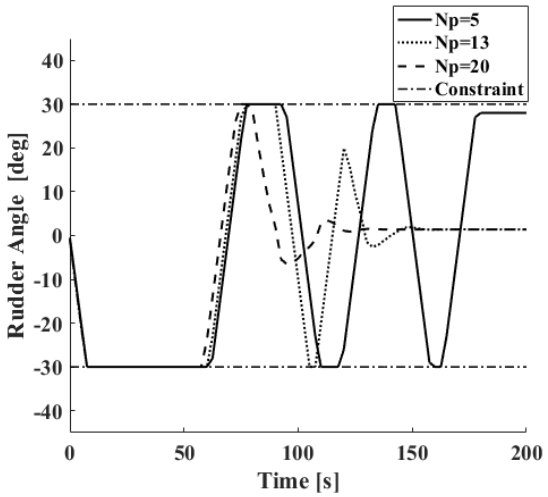

Figure 5: Rudder angle deflections and operating constraint bound for different number of prediction horizon

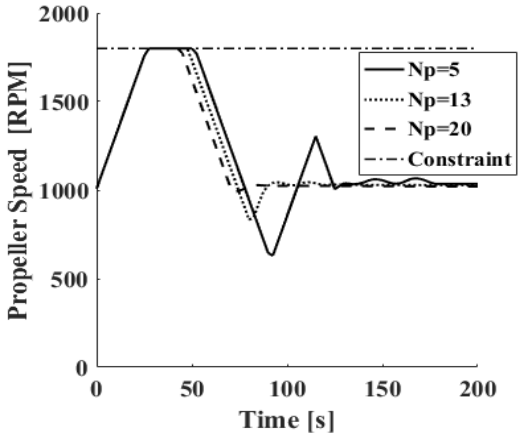

Figure 6: Propeller speed and high limit constraint for different number of prediction horizon

MPC operates such a model based manner that faced with nonlinear systems, prediction may be incorrect especially in chaotic models because of nonlinear states. This fact as well as interactions caused inability of whole vehicle motion control simulations show MPC succeed when AUV reaches desired speed with corresponding pitch angle as mentioned before but according to "Figure 7" there are some interactions which is arisen from coupled states but all constraints are fulfilled.

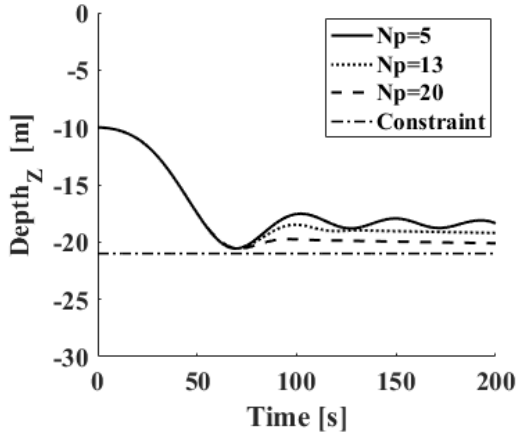

Figure 7: Depth interaction while speed regulation and constraint depth

5. Summary and conclusions

Since enormous exciting plant restrictions on inputs, states and outputs such as low and high ranges, variation rate, saturations and etc., MPC is known as powerful strategy for industrial control. In this paper we introduced an AUV nonlinear dynamic model and after linearization we applied MPC to solve speed regulation problem in horizontal plane. Our approach found response so feasible signals that all restrictions on control signals contain high and low limit bound, variation rate of rudder deflection and propeller speed is considered. Besides other state restrictions or interactions like depth of vehicle are satisfied too. Indeed, researchers can focus on using of the MPC to decoupling AUV dynamic model in future works or implementing it to multitask motion system or improve reliability. In addition, using the offset-free control strategy [24] can involve ocean current as disturbance and in order to guarantee stability, reference governor approach [22] leads to convergence and avoids infeasibility issues.

References

[1] Blidberg, D. R., ‘‘The development of autonomous underwater vehicles (AUV); a brief summary,’’ IEEE ICRA, vol. 4, 2001

[2] Wernli, R.L., ‘‘AUVs-a technology whose time has come,’’ Underwater Technology, Proceedings of the 2002 International Symposium on. IEEE, 2002.

[3] Danson, E. F., ‘‘AUV tasks in the offshore industry,’’ Technology and Applications of Autonomous Underwater Vehicles, Griffiths, G.(ed). Taylor and Francis, London, pp. 127-138, 2003.

[4] Vervoort, J. H. A. M., *Modeling and control of an unmanned underwater vehicle*, 2009.

[5] Fossen, T. I., *Handbook of marine craft hydrodynamics and motion control*, John Wiley & Sons, 2011.

[6] Tang, S. C., *Modeling and simulation of the autonomous underwater vehicle*, Autolycus (Doctoral dissertation, Massachusetts Institute of Technology), 1999.

[7] Wadoo, S., Kachroo, P., *Autonomous underwater vehicles: modeling, control design and simulation*, CRC Press (2016).

[8] Valentinis, F., Donaire, A., Perez, T., ‘‘Energy-based motion control of a slender hull unmanned underwater vehicle,’’ Ocean Engineering, vol. 104, pp. 604-616, 2015.

[9] Yoshida, K., El-Nemr, M., Yamshita, Y., ‘‘Pitching stability analysis and control for underwater maglev linear motor vehicle ME02,’’ Power Electronics and Motion Control Conference, EPE-PEMC 2006. 12th International. IEEE, 2006.

[10] Elnashr, G. A., ‘‘Performance and stability analysis of an autonomous underwater vehicle guidance and Control,” proceding international conference of modeling, identification and control (ICMIC), pp. 67-73, 2013.

[11] Bagnia, S.,Aggarwal, N., ‘‘Depth control of autonomous underwater vehicle using MPC, ’’ international journal of research, vol. 2, no. 8, 2015.

[12] Fernández, D. C.,‘‘Model Predictive Control for Underwater Robots in Ocean Waves (master’s thesis),’’ Oregon State University, 2015.

[13] Johansen, T. A., Perez, T., Cristofaro, A., ‘‘Ship collision avoidance and COLREGS compliance using Simulation-based control behavior selection with predictive hazard assessment,’’ 2016.

[14] Zhao, Y., Li, W., Shi, P., ‘‘A real-time collision avoidance learning system for Unmanned Surface Vessels,’’ Neurocomputing, vol. 182, pp. 255-266, 2016.

[15] Akçakaya, H., Gören Sümer, L., ‘‘Robust control of variable speed autonomous underwater vehicle,’’ Advanced Robotics, vol. 28, no. 9, pp. 601-611, 2014.

[16] Franze, G., Lucia, W., ‘‘A Receding Horizon Control Strategy for Autonomous Vehicles in Dynamic Environments,’’ IEEE Transactions on Control Systems Technology 24, no. 2, pp. 695-702, 2016.

[17] Franzè, G., Lucia, W., ‘‘The obstacle avoidance motion planning problem for autonomous vehicles: A low-demanding receding horizon control scheme,’’ Systems & Control Letters, vol. 77, pp. 1-10, 2015.

[18] Kasdin, N. J., ‘‘Dynamics of Particles and Rigid Bodies [Book Review],’’ IEEE Control Systems, 26, no. 6, pp. 115-116, 2006.

[19] Healey, A. J., Lienard, D., ‘‘Multivariable sliding mode control for autonomous diving and steering of unmanned underwater vehicles,’’ IEEE journal of Oceanic Engineering, vol. 18, no. 3, pp. 327-339, 1993.

[20] Wang, L., *Model predictive control system design and implementation using MATLAB®*, Springer Science & Business Media, 2009.

[21] D.Q. Mayne, J.B. Rawlings, C.V. Rao, and P.O.M. Scokaert., ‘‘Constrained model predictive

control: Stability and optimality'' Automatica, 36(6):789–814, 2000.
[22] Aghaei, S., Sheikholeslam, F., Farina, M., Scattolini, R., ''An MPC-based reference governor approach for offset-free control of constrained linear systems,'' International Journal of Control, vol. 86, no. 9, pp. 1534-1539, 2013.
[23] Gilbert, E., &Tan, K. (1991). Linear systems with state and control constraints: The theory and application of maximal output admissible sets. IEEE Transactions on Automatic Control, 36, 1008–1020.
[24] Aghaee, S., Zakeri, Y., Sheikholeslam, F., ''Offset-free control of constrained linear systems using model predictive control,'' 2008 IEEE International Symposium on Industrial Electronics. IEEE, 2008.

INTERNATIONAL JOURNAL OF
COASTAL & OFFSHORE ENGINEERING
IJCOE No. 3/Summer 2016 (35-41)

Analysis of Band Curvature in Asymmetrical Rolling Process by FEM Method

Hassan Sayyaadi [1], Ramin Yekta[2], Abolfazl Motekallem[3]

[1]*Ph.D, Sharif University of Technology/ Department of Mechanical Engineering; Sayyaadi@sharif.edu*
[2]*M.SC Student, Sharif University of Technology/ Department of Mechanical Engineering; Yekta_Ramin@mech.sharif.edu*
[3] *M.SC Student, Sharif University of Technology/ Department of Mechanical Engineering; Motekallem_Abolfazl@mech.sharif.edu*

ARTICLE INFO

Article History:
Received: 8 Mar. 2016
Accepted: 15 Sep. 2016

Keywords:
Asymmetrical rolling, Finite Element Method, Radii ratio, Speed ratio, Sheet Curvature

ABSTRACT

Today, the rolled products, i.e. sheet, plate and foil is used in marine applications, including platforms, hatch covers, mast, hulls of boats and superstructures on pleasure boats and the bridges and superstructures of passenger ships and merchant ships. In this paper, simulation of asymmetric cold rolling is presented by using explicit analysis procedure. In asymmetric cold rolling, the workpiese if often bent downwards or upwards. A two dimensional explicit dynamic finite element model with adaptive meshing technique has been employed to simulate asymmetrical condition are here due to different roll radii. To validate the simulation, the results of simulation and experiment are compared. Effects of asymmetry due to roll radii ratio and speed ratio mismatch on sheet curvature variations are discussed. Finally, optimum roll speed ratio in various of roll radii ratio could be found to produce flat sheet.

1. 1. Introduction

Rolled products, i.e. sheet, plate and foil constitute almost 50% of all aluminium alloys used. Sheet is also used extensively in marine applications, including offshore platforms, superstructures and hulls of boats furthermore the sheet is used in building for roofing and siding, in transport for airframes, road and rail vehicles. Plate is used for airframes, military vehicles and bridges, ships superstructures, cryogenic and chemical vessels and as tooling plate for the production of plastic products. Foil applications outside packaging include electrical equipment, insulation for buildings, lithographic plate and foil for heat exchangers. Therefore, Theoretical and experimental studies have been carried out to investigate the deformation mechanics of asymmetric plane strain rolling. Sachs and Klingler [1] used the slab method to develop a homogeneous deformation model. They concluded that there exists a region where the frictional forces on the driven and undriven rolls act on the strip in opposite directions and identified it as the region of cross shear. Holbrook and Zorowski [2] extended the earlier model to include nonsymmetry of the roll pressure distribution. On a twin roll driven asymmetrical rolling mill Kennedy and Slamar [3] rolled steel strip, and Buxton and Browning [4] rolled strips of plasticine. Their results show that under certain conditions a decrease in roll force of as high as 40% is possible. Johnson and Needham [5] carried out a few experiments using lead as a model material to study curvature. They developed analytical models based on the upper bound method [6] and the slip line field analysis [7] to predict strip curvature. Kiuchi and Hsiang [8] used an upper bound technique for calculating curvature in plates by rolls of different diameters and roll speed mismatch. Pospiech [9] investigated the effect of thickness reductions on curvature developments for the asymmetrical rolling conditions. Richelsen [10] investigated the influence of the degree of deformation and the initial thickness on bending of the asymmetrically rolled strip using FEM. Shivpuri et al. [11] used an explicit integration finite element method to investigate curling due to speed mismatch asymmetrical rolling. A similar FEM simulation was also performed by Lu et al. [12]. Hwang and Chen [13] made an attempt to analyze the asymmetrical rolling by using the stream function method. Salimi and Sassani [14] Pietrzyk et al. [15] simulated the asymmetrical plate rolling by the finite element method in a steady state condition. Hamuzu et al. [16] studied the asymmetrical rolling process in unequal

surface speed conditions using the rigid perfectly plastic model.

2. The Finite Element Models

Many three dimensional models of the steady state processes are based on the flow formulation in a fixed mesh. The finite element mesh used in flow formulation is usually fixed in a Eulerian system. Thus, Eulerian elements undergo no distortion due to material motion and cannot properly predict the outgoing material shape, as the treatment of moving boundary and interface is difficult with this method. To follow the material movement and to estimate the plate curvature Lagrangian meshes are more convenient. Unfortunately for simulation of processes such as asymmetrical rolling, where the material is severely deformed and the outgoing plate may be deformed in an unexpected shape.

3. Modeling of Asymmetric Rolling

Fig. 1 shows the schematic of asymmetric rolling. The figure also shows the positions of the neutral points. The deformation zone is divided into three stages. In this article, the indexes 1 and 2 were used for top rolls and bottom rolls, respectively. In stage (I), the friction force applied on the top and the bottom surfaces are coincided with the flow of materials. The opposite situation is seen in stage (III). In stage (II), the friction force on the top and the bottom surface of the sheet are against each other, i.e., the shear zones are created. Where R_1 and R_2 are the top and the bottom rolls radius, h_i and h_0 are the initial and final sheet thickness. The Hollowman elastic plastic equation was used to describe the behavior of sheets (i.e., $\sigma = c\varepsilon^n$, where σ was stress, ε the strain and n the strain hardening constant, c and n were material constants). The material constants used were c = 162.3 MPa, n = 0.0353 [17]. All the simulations were carried out with aluminum 1050P (E = 69 GPa, σ_y = 69 MPa) and for the sheet width of 100 mm.

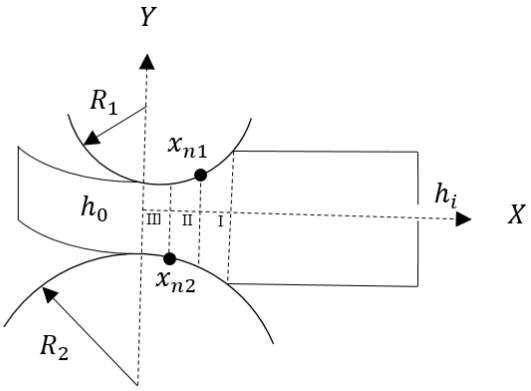

Fig. 1. Schematic of asymmetric rolling.

μ the coefficient of friction, m the friction factor. The magnitude of m corresponding to various coefficients of friction was obtained by Eq. (1), i.e.,

$$\mu = \frac{m}{1+0.5\pi+\cos^{-1}(m)+\sqrt{1-m^2}} \quad (1)$$

The rolls were rotated by the constant angular velocity of ω about their axes. No lateral transitions were assumed for the rolls in the analyses. The sheet velocity equaled to the x-component of the roll surface velocity. The sheet was fixed along its width. The latter condition caused the sheet to be moved in the x-direction only. The sheet was allowed to deflect in any direction at the exit. In this study, ABAQUS explicit analyses were used to simulate the symmetric asymmetric rolling [18].

4. Validation of The Simulation Results

4.1 Mesh Dependency Study

Mesh dependency study was carried out and it has been demonstrated that further increasing in mesh density makes little difference on the results. In order to set up a grid independent solution, numerical simulations have been conducted for different meshes and the optimum mesh consisted of 6250 quadrilateral elements. The number and type of mesh elements have been selected in an iterative solution with a minimal time step to obtain an accurate solution. The same geometry and mesh elements, as well as initial and boundary conditions, were used for all numerical simulations. Here, the mesh refinement sensitivity is summarized in Table 1 and Fig. 2,3. According to the findings, the refined mesh was chosen for the rest of the simulations.

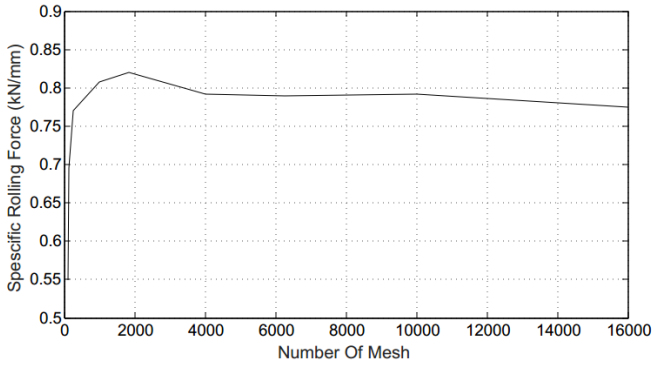

Fig. 2. Mesh refinement sensitivity

Table 1: Mesh refinement sensitivity

Mesh Case	Number of Element	Sheet Force (KN/mm)
(1)	100	0.549
(2)	125	0.695
(3)	250	0.769
(4)	1000	0.808
(5)	1850	0.820
(6)	4000	0.791
(7)	6250	0.780
(8)	10000	0.797
(9)	16000	0.775

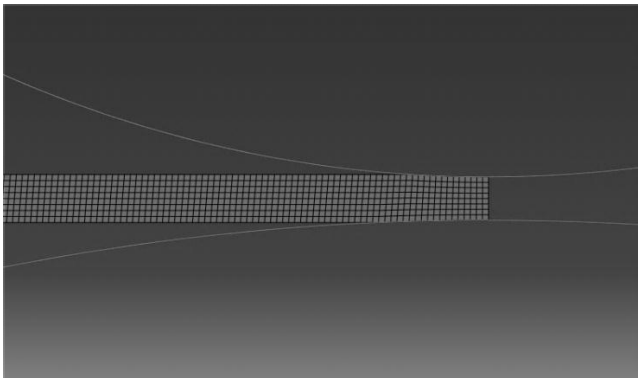

Fig. 3. Two Dimensional Grid

4.2 Validation of The Simulation Results

The rolling parameters obtained from the simulations, were compared with the experimental studies of references [17] and theoretical study of [17,19]. The material constants and the condition of the simulation were similar to those used in references [17,19]. To validate the rolling force, the experimental results of reference [17] was employed (see Fig. 4). The effects of reduction on rolling force are depicted in Fig. 4. The analytical results of reference [17,19] also showed in the graph. Good agreements were obtained between the simulation results and the experimental results.

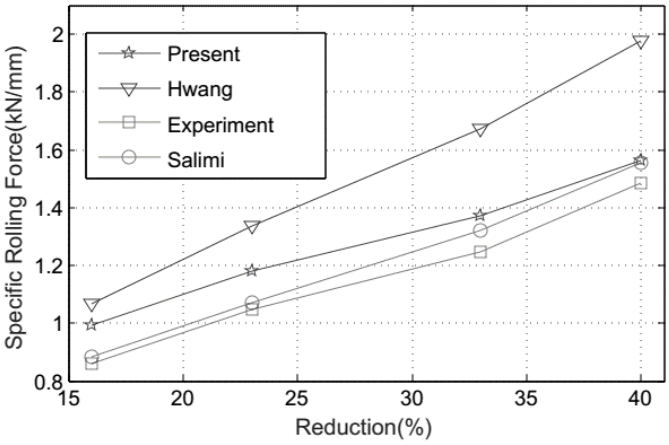

Fig. 4. Comparison of rolling force predicted by the present model with other researchers, Result: ($R_u = 50mm$, $R_l = 105mm$, $m_u = m_l = 0.359$, $h_i = 2mm$, $V_A = 1.05$, $\sigma_{x1} = \sigma_{x0} = 0$)

5. Specifications of Simulated Models

All the simulations were performed by assuming the constant friction coefficient of 0.359 for the top and the bottom sheet surfaces. In addition, the linear velocity of the top roll was presumed to be constant and equaled to V = 0.556 m/s. The top roll radius was assumed to be constant and equaled to $R_u = 105\ mm$. The precentage reduction is %10 selected for all simulations. The asymmetry was produced due to change of linear velocity and radius of the bottom rolls. In this paper, the curvature is positive when the Y axis is in the negative direction that is shown in Fig. 5.

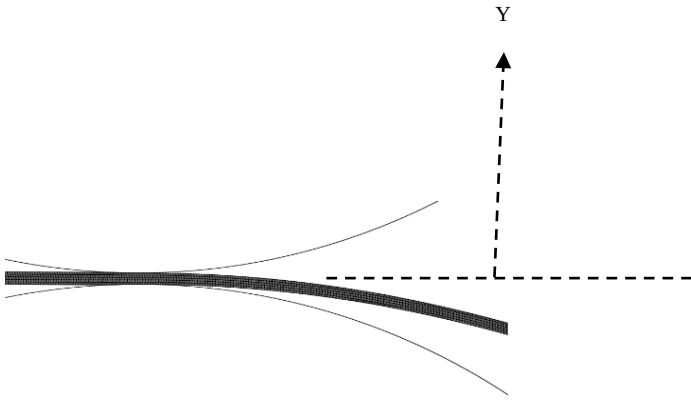

Fig. 5. The schematic of positive curvature

6. Application of Rolled Aluminum in Marine Industries

Rolled aluminum sheet and plates are a remarkably versatile material. The major incentive for employing aluminum is its weight saving compared to steel, because it is common practice to use wieldable aluminum alloys having strengths approaching or comparable to mild steel, equal strength structures can be designed to a weight saving of 55 to 67 percent. However, to compensate for the lower modulus of elasticity of aluminum and to conform to normal deflection limitations, a somewhat lower, but substantial, reduction in weight is usually obtained. Its applications are too many to list completely. As shown in Fig. 6 is rolled aluminum is used in deckhouses, hatch covers of commercial ships, shell plating, round bilge, superstructures of large merchant and military ships, small boat hulls, aircraft skins, bulkheads, as well as in equipment items, such as ladders, railings, gratings, windows, doors and in marine platforms used in Helidecks, Multipurpose modules, Accommodation modules, Cladding, Fire blast wall, Mud mats, Internal fittings, Link bridges, Access systems and Air filtration systems.

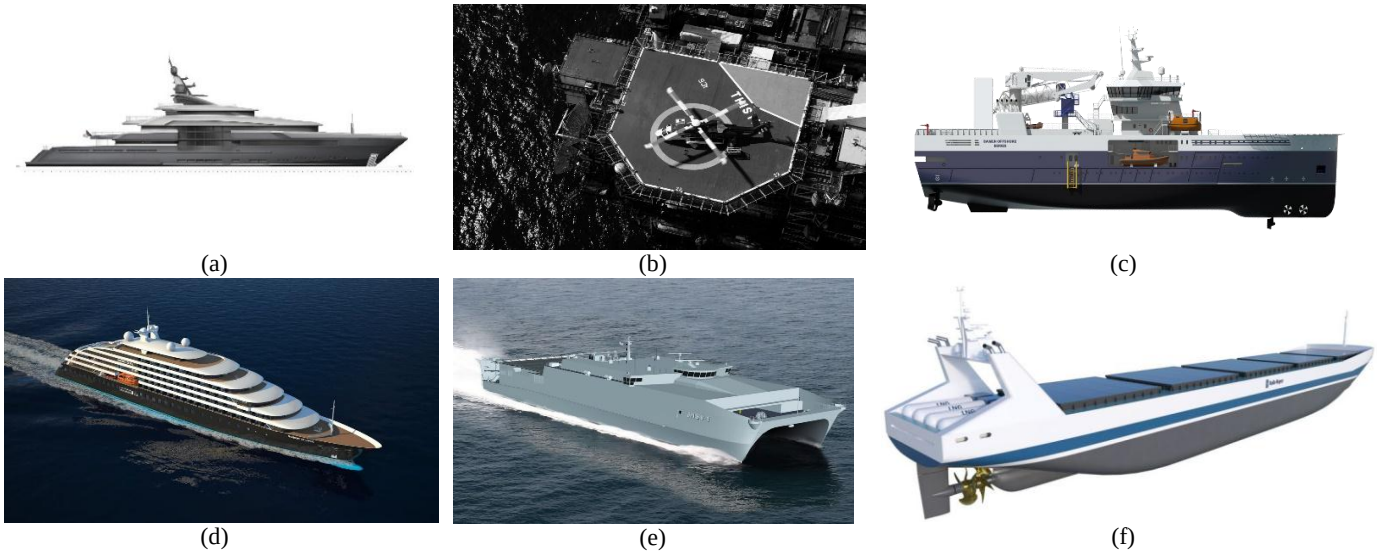

(a) (b) (c)

(d) (e) (f)

Fig. 6. Application of Rolled Aluminum, (a). Small Boat Hulls, (b). Helideck of Marine Platform, (c). Superstructures of Merchant Ships, (d). Accommodation of Cruise Ships, (e). Shell Plating, (f). Hatch Covers of Commercial Ships

7. Results and Discussion

It should be noted that although reducing the load and torque is one of the advantages in the asymmetric rolling, however, producing the sheet with no curvature is preferable. It is also advisable to produce the zero sheet curvature with lower load and torque. Therefore, the study was further conducted to found the optimum linear velocity in order to create the zero sheet curvature in the asymmetric rolling. Fig. 9 to Fig. 14 shows the variation of sheet curvature with the linear velocity ratio for six radii ratio of 1,1.01,1.02,1.03,1.04 and 1.05.

First, one can imagine that the sheets must be bent to roll that has a lower speed. Since the linear velocity of the upper roller surface is less than the linear velocity of the lower roller surface must be bent upward sheet. As the velocity vector of lower surface of sheet greater than the velocity vector of upper surface of sheet therefore the sheet bent upward that is shown in Fig. 7. But unlike the first impression by increasing the radii ratio (or speed ratio) sheet is bent downward, but with greater this ratio, the sheet is bent upward.

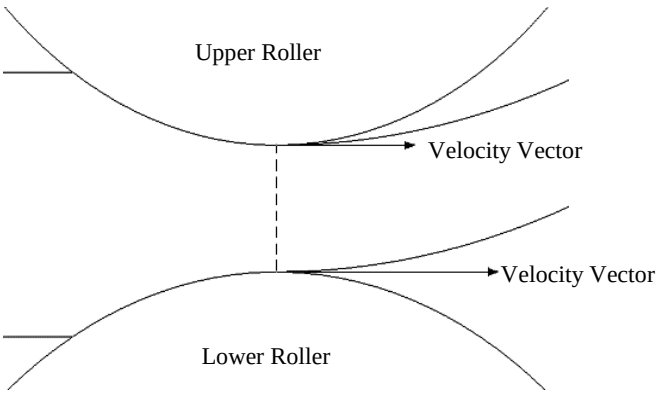

Fig. 7. Velocity Vector of Surface

For interpretation must also consider the position of the neutral point, the neutral point is the point where linear velocity of the roller and sheet is equal. Assume that the radii ratio (or speed ratio) is equaled r_A when the linear velocity of the upper roller is equaled V then the linear velocity of the lower roller is $V \times r_A$ therefore the upper neural point velocity is V and the lower neural point velocity is $V \times r_A$. When r_A is very small in asymmetric and symmetric mode, almost at the same time, a specified length of sheets to be rolled. So it can be concluded that the average speed is equal in both cases. In Fig. 8 A and C points are neural point in asymmetric mode, Similarly B and E points are neural point in the symmetric mode. As in the case of symmetrical upper and lower roller speed is equal, it can be concluded that in the case of symmetric mode the linear velocity on the line BE is constant and equal to V.

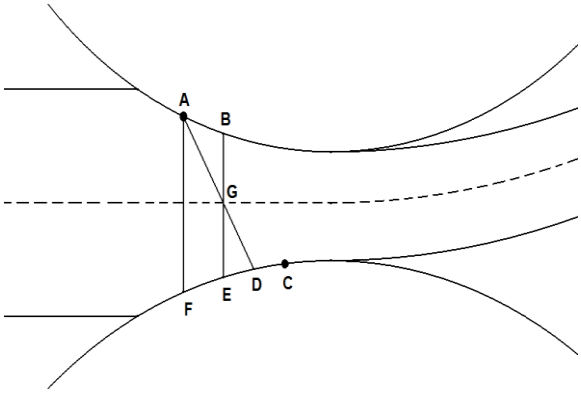

Fig. 8. Schematic of Neural Point in Symmetry and Asymmetry Mode

Since the speed of symmetric and asymmetric mode in the middle of the sheet should be equal, then the velocity of G point in two modes is V and equal. Because the velocity of the A point that it is the neural

point of the upper roller, is equal V and the sheet thickness is very small it can be assumed that the velocity profile of the sheet is linear. By drawing lines AG and extending it to point D can be concluded that the speed of points on the line AD is equal to V.

According to the previous definitions to know that the velocity of the F point must be less than the velocity of the D point, Because the F point before D point. So we conclude that A point on AF line and on top of the sheet are rated more velocity. So we can say that the average velocity of the upper points more than the average velocity of the lower points that is located on sheet. So the average velocity on each side that is more than sheet bent to the other side.

With increasing more, the radii ratio the horizontal distance between two neural point increased and average velocity difference between the top and bottom of the sheet surface increased to reach its maximum. In this case, the curvature of the sheet in the downward direction to reach its maximum value.

But then with more elevated the radii ratio (or speed ratio) the neutral point almost proved to be and no other significant displacement. But while more increasing the radii ratio (or speed ratio) the velocity average constantly increased. This process continues to be almost the average velocity of the rollers will be together and in radii ratio (or speed ratio) special and sheet almost horizontally and without inflection is out.

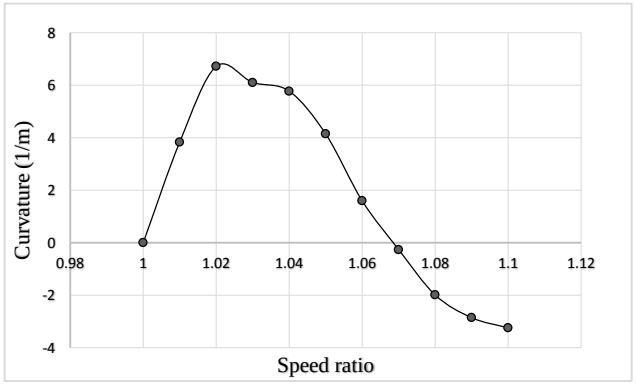

Fig. 9. Sheet Curvature Against Speed Ratio for Radii Ratio 1 ($R_u = 105mm, R_l = 105mm, m_u = m_l = 0.359, h_i = 2mm, \sigma_{x1} = \sigma_{x0} = 0, r = 10$)

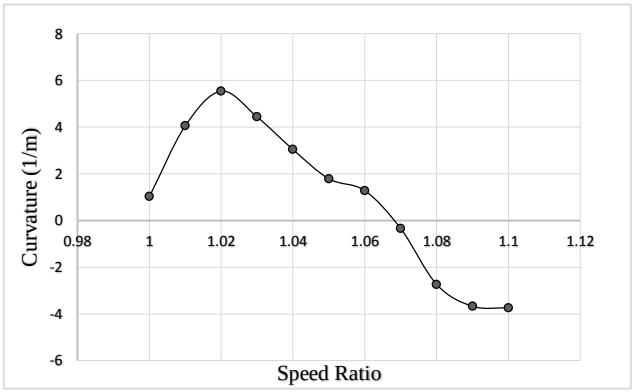

Fig. 10. Sheet Curvature Against Speed Ratio for Radii Ratio 1.01 ($R_u = 105mm, R_l = 106.05mm, m_u = m_l = 0.359, h_i = 2mm, \sigma_{x1} = \sigma_{x0} = 0, r = 10$)

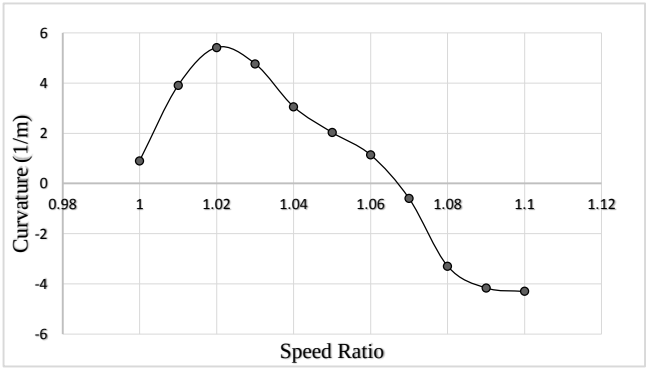

Fig. 11. Sheet Curvature Against Speed Ratio for Radii Ratio 1.02 ($R_u = 105mm, R_l = 107.10mm, m_u = m_l = 0.359, h_i = 2mm, \sigma_{x1} = \sigma_{x0} = 0, r = 10$)

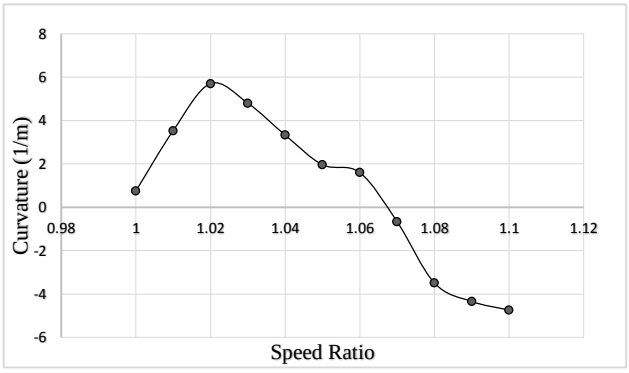

Fig. 12. Sheet Curvature Against Speed Ratio for Radii Ratio 1.03 ($R_u = 105mm, R_l = 108.15mm, m_u = m_l = 0.359, h_i = 2mm, \sigma_{x1} = \sigma_{x0} = 0, r = 10$)

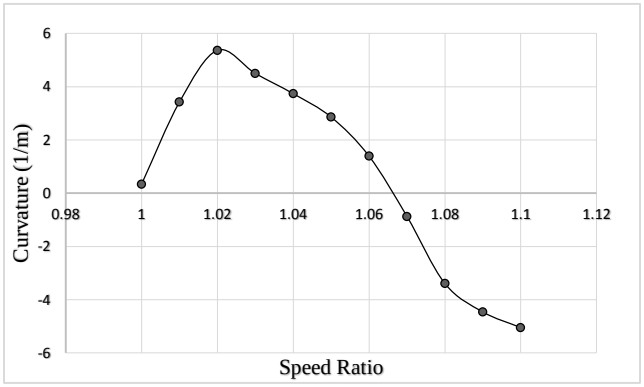

Fig. 13. Sheet Curvature Against Speed Ratio for Radii Ratio 1.04 ($R_u = 105mm, R_l = 109.20mm, m_u = m_l = 0.359, h_i = 2mm, \sigma_{x1} = \sigma_{x0} = 0, r = 10$)

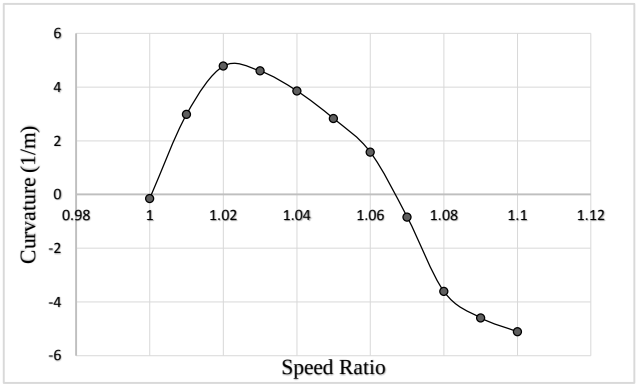

Fig. 14. Sheet Curvature Against Speed Ratio for Radii Ratio 1.05 ($R_u = 105mm, R_l = 110.25mm, m_u = m_l = 0.359, h_i = 2mm, \sigma_{x1} = \sigma_{x0} = 0, r = 10$)

Conclusions

In this paper, the asymmetric rolling was investigated and analyzed by the finite element method. Effects of asymmetry due to roll radii ratio and speed ratio mismatch on sheet curvature variations are discussed. The simulation results agreed well with the past experiments and theoretical studies. The following conclusions can be drawn:

- For each radii ratio, an optimum speed ratio to produce flat sheet calculated that is shown in Table 2.

Table 2: Optimum Speed Ratio

Radii Ratio	1	1.01	1.02	1.03	1.04	1.05
Speed Ratio	1.06831	1.06828	1.06692	1.06732	1.06633	1.06663

- By increasing the radii ratio, the optimum speed ratio which the sheet has zero curvature is reduced.

- As can be seen in Fig. 9 to Fig. 14 by increasing the radii ratio, the maximum sheet curvature is reduced.

List of Symbols (Optional)

E	Modulus of elasticity
R_1	Top roll radius
R_2	Bottom roll radius
R_u	Top roll radius
R_l	Bottom roll radius
μ	Friction coefficient
m	Friction factor
m_u	Top roll friction factor
m_l	Bottom roll friction factor
V_A	Speed ratio
h_i	Initial thickness
h_o	Output thickness
r	Percentage reduction

Greek symbols

σ	Stress
ε	Strain

References

[1] G. Sachs, L.J. Klingler, The flow of metals through tools of circular contour, J. Appl. Mech. 14 (1947) 88.
[2] L. Holbrook, C.F. Zorowski, Effects of non symmetry in strip rolling, J. Eng. Ind. B88 (1966) 401.
[3] G.E. Kennedy, F. Slamar, Turn up and turn down in hot rolling, in: Iron and Steel Engineer Yearbook, 1958, p.233.
[4] S.A. Buxton, S.C. Browning, Turn up and turndown in hot rolling: a study on a model mill using plasticine, J. Mech. Eng. Sci. 14 (1972) 245.
[5] W. Johnson, G. Needham, an experimental study of asymmetrical rolling, in: Applied Mechanics Convention, Institute of Mechanical Engineers, Cambridge, UK, 1966.
[6] W. Johnson, G. Needham, Further experiments in asymmetrical rolling, Int. J. Mech. Sci. 8 (1972) 443.
[7] P. Dewhurst, I.F. Collins, W. Johnson, A theoretical and experimental investigation into asymmetrical hot rolling, Int. J. Mech. Sci. 16 (1974) 389.
[8] M.M. Kiuchi, S. Hsiang, Analytical model of asymmetrical rolling process of sheets, in: Proceedings of the 14th NAMRC, Society of Manufacturing Engineers, Minneapolis, 1986, p. 384.
[9] J. Pospiech, a note on the influence of some factors affecting curvature on the flat rolling of strip, J. Mech. Work. Tech. 15 (1987) 64.

[10] A.B. Richelsen, Elastic–plastic analysis of the stress and strain distributions in asymmetric rolling, Int. J. Mech. Sci. 39 (1997) 1199.
[11] R. Shivpuri, P.C. Chou, C.W. Lau, Finite element investigation of curling in nonsymmetrical rolling of sheet, Int. J. Mech. Sci. 30 (1988) 625.
[12] L.-S. Lu, O.-K. Harrer, W. Schwenzfeier, F.D. Fischer, Analysis of the bending of the rolling material in asymmetrical sheet rolling, Int. J. Mech. Eng. Sci. 42 (2000) 49.
[13] Y.M. Hwang, T.H. Chen, Analysis of asymmetrical rolling by stream function method, JSME 39 (1996) 598.
[14] M. Salimi, F. Sassani, Modified slab analysis of asymmetrical plate rolling, Int. J. Mech. Sci. 44 (2002) 1999–2023.
[15] M. Pietrzyk, K. Wilk, H. Kusiak, Steady state FEM simulation of the strip bending in asymmetrical rolling process, in: Proceedings of the Metal Forming 93, Krynica, 1993, pp. 50–55.
[16] S. Hamuzu, K. Yamada, T. Kawanmi, et al., Rigid plastic finite element analysis of asymmetrical rolling, in: D.R.J. Owen, E. Hinton, E. Onate (Eds.), Computational Plasticity, Pineridge Press, Swansea, 1987, pp. 1087–1096.
[17] Y.M. Hwang, G.Y. Tzou, Analytical and experimental study on asymmetric sheet rolling, Int. J. Mech. Sci. 39 (1997) (1997) 289–303.
[18] H.D. Hibbitt, B.I. Karlson, D. Sorensen, HKS Inc. Rolling of Thick Plates (1.3.6), Abaqus/Explicit 6.4, 2004.
[19] M. Salimi, A. Forghani, Prediction of product curvature in rolling with asymmetric condition, in: The Seventh ISME Annual Conference, Zahedan, Iran, April 14–16, 1999, pp. 1485–1493 (in Persian).